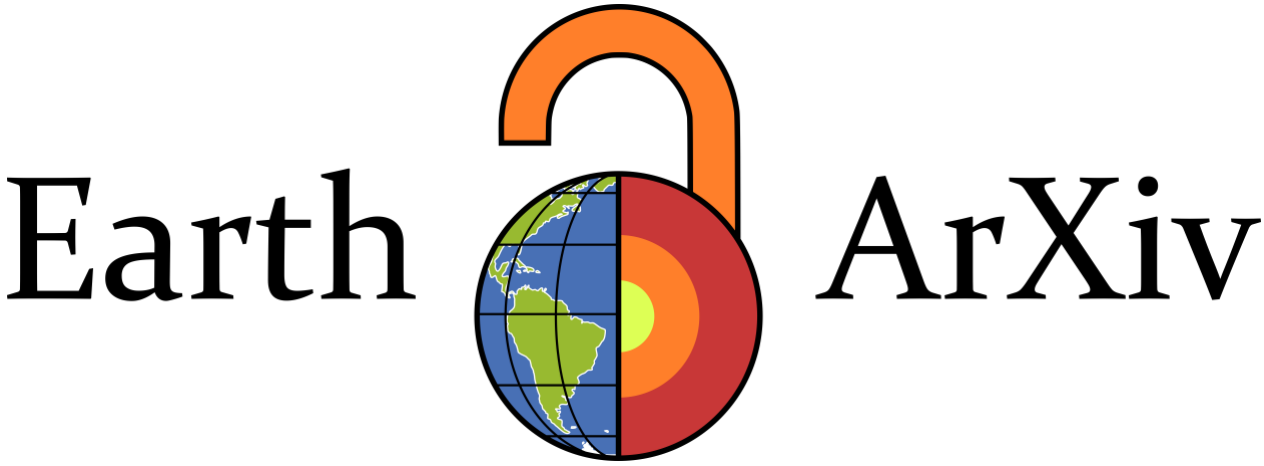


This is a non-peer-reviewed preprint submitted to EarthArXiv.

This manuscript has been submitted for publication in *Science Advances*. Please note the manuscript has yet to be formally accepted for publication. Subsequent versions of this manuscript may have slightly different content. If accepted, the final version of this manuscript will be available via the 'Peer-reviewed Publication DOI' link on the right-hand side of this webpage. Please feel free to contact any of the authors; we welcome feedback.

Title: Observational uncertainty is the primary source of climate uncertainty in impacts projections

Authors: Kevin Schwarzwald*[1,2], Nathan Lenssen[3,4], Tom Bearpark[5,6], Alia Bonanno[7], Radley Horton[1,2], Gernot Wagner[7]

Affiliations:

[1]Columbia Climate School, Columbia University; New York, NY 10025, USA.

[2]Lamont-Doherty Earth Observatory of Columbia University; Palisades, NY 100964, USA.

[3]Colorado School of Mines; Golden, CO 80401, USA.

[4]NSF National Center for Atmospheric Research; Boulder, CO 80307, USA.

[5]Land, Environment, Economics and Policy Institute, University of Exeter; Exeter, EX4 4PU, UK.

[6]Grantham Research Institute on Climate Change and the Environment, London School of Economics; London, WC2A 2AE, UK.

[7]Columbia Business School, Columbia University; New York, NY 10027, USA.

*Corresponding author. Email: kevin.schwarzwald@columbia.edu

Abstract: Projections of future climate damages underpin environmental policy and risk management but depend on inherently uncertain climate data. Uncertainty in historical climate observations, used to train impact models and calibrate climate projections to the observed record, is rarely considered. We show this "observational uncertainty" contributes more than the spread across or within global climate models to projections of mortality, GDP per capita growth, and payroll. Most of this uncertainty stems from training impact models; even small differences in historic weather estimates can cause large differences in projected damages. Incorporating this uncertainty increases the spread in climate uncertainty by up to 300%, highlighting the importance of impact model design and the need for better constraints on observations, and implying a higher Social Cost of Carbon.

Projections of the socioeconomic impacts of climate change are increasingly used to understand and prepare for climate risks, yet the *climate* uncertainties in these studies are often underestimated (*1*). Statistical projections of the impacts of climate change on society typically fit an econometric model relating a historical weather variable to a socioeconomic outcome, creating a `dose-response function', and then project damages into the future using expected changes in that weather variable under increased greenhouse gases (*2–6*). This class of models is used by financial actors and policymakers to estimate future large-scale climate risks (*7*) and by researchers to estimate the Social Cost of Carbon (SCC) used in cost-benefit analyses and regulatory policymaking in North America and Europe (*6*, *8–11*).

Impact projections are inherently uncertain. No study perfectly recovers the true dose-response function, and no single authoritative projection of future climate conditions exists. How faithfully this uncertainty is represented matters for policy. Because damages tend to be non-linear and society is risk averse, both the upper tail and the central estimate are used to determine the Social Cost of Carbon and motivate precautionary adaptation (*11–14*).

A major driver of uncertainty in impact projections is the climate data itself, through two primary pathways. First, future climate projections come from ensembles of Global Climate Models (GCMs), whose uncertainties are well-documented in the climate science literature. They come from three sources (*15–17*): scenario uncertainty in future emissions and forcings, model uncertainty in how the Earth system responds, and internal variability from the climate's intrinsic chaos. Second, estimates of historical weather conditions are used both to fit the dose-response function and to bias-correct and downscale the GCM output — adjusting it toward observations and to finer spatial resolution (*2*, *18*) (fig. S1). Uncertainty in this historical record has not been systematically accounted for in the climate impact literature to date, leading to a major gap in our understanding of the true uncertainty in our projections. Here, we fill that gap with a large-scale analysis of the uncertainty in future climate damage projections due to imperfect estimates of historical climate.

This uncertainty in the historical global weather record can be substantial. The location of ground-based weather stations is biased towards wealthier regions and populated and accessible areas, systematically undersampling developing countries and regions with complex topography (*19–23*). Additionally, existing station networks may provide restricted access to data for economic or legal reasons (*2*) and/or may suffer from temporal gaps in their records due to quality control issues, funding lapses, or conflict (*21*, *24*). Gridded data products designed to plug these gaps, including complex high-resolution weather models constrained by observations known as ‘reanalyses’, differ in how they assimilate varied subsets of available data sources, producing different estimates of historical conditions at the same locations (*18*). For example, over the late 20th century, the population-weighted mean difference between the European Centre for Medium-Range Weather Forecasting (ECMWF)'s ERA5 (*25*) and NASA's MERRA-2 (*26*), two leading reanalyses, is 0.7°C, 1.5°C, and 1.9°C over the globe, in Pakistan, and in Guatemala, respectively. These differences increase for extremes, reaching 1.2°C, 2.4°C, and 2.9°C respectively for the 99th percentile of the daily temperature distribution in the same locations. As of 2026, there are three global, continuously updating reanalysis products publicly available (ERA5, JRA-3Q (*27*), and MERRA-2) and another half dozen statistically interpolated or blended gridded data products commonly used in climate impacts research, in addition to older reanalyses still in use.

Importantly, the choice of which gridded weather record to use in projections of climate impacts tends to either be *ad hoc* or based on criteria other than a product's suitability as a historical "ground truth". For example, the Global Meteorological Forcing Dataset for Land Surface Modeling (GMFD) (*28*) is frequently used in impacts analyses (*29–31*), despite being based on an outdated (*32*) reanalysis system with few evaluations, because it is the dataset used to bias-correct and downscale NASA's NEX-GDDP product (*33*), a commonly-used set of GCM projections. Many studies do not justify their choice of historical gridded data product or show only that the chosen product appears reasonable for their purpose without evaluating whether a different one would be better suited.

Evaluations of the fitness-for-purpose of historical weather data increasingly exist (*34–39*). However, these studies tend to be localized and specific to particular metrics and crucially do not produce a self-consistent ranking of gridded weather records. More broadly, such evaluations are not always feasible due to a paucity of independent verification datasets, especially in poorer regions likely to experience the worst impacts of climate change (*21*, *29*). Thus, even when evaluations are available, choosing a clear 'best' product to use in climate impacts research is difficult, if not impossible.

In other words, the inability to know the true historical weather conditions is a critical fourth source of climate uncertainty in projections of climate impacts, beyond scenario, model, and internal uncertainty introduced above. The influence of this 'observational uncertainty' on the projected range of climate damages depends on how this uncertainty propagates to estimates of a population's historic exposure to weather conditions, the bias-correction and downscaling of future climate projections, and how these pathways interact with climate impact modeling decisions, including the functional form of the impact model (fig. S1).

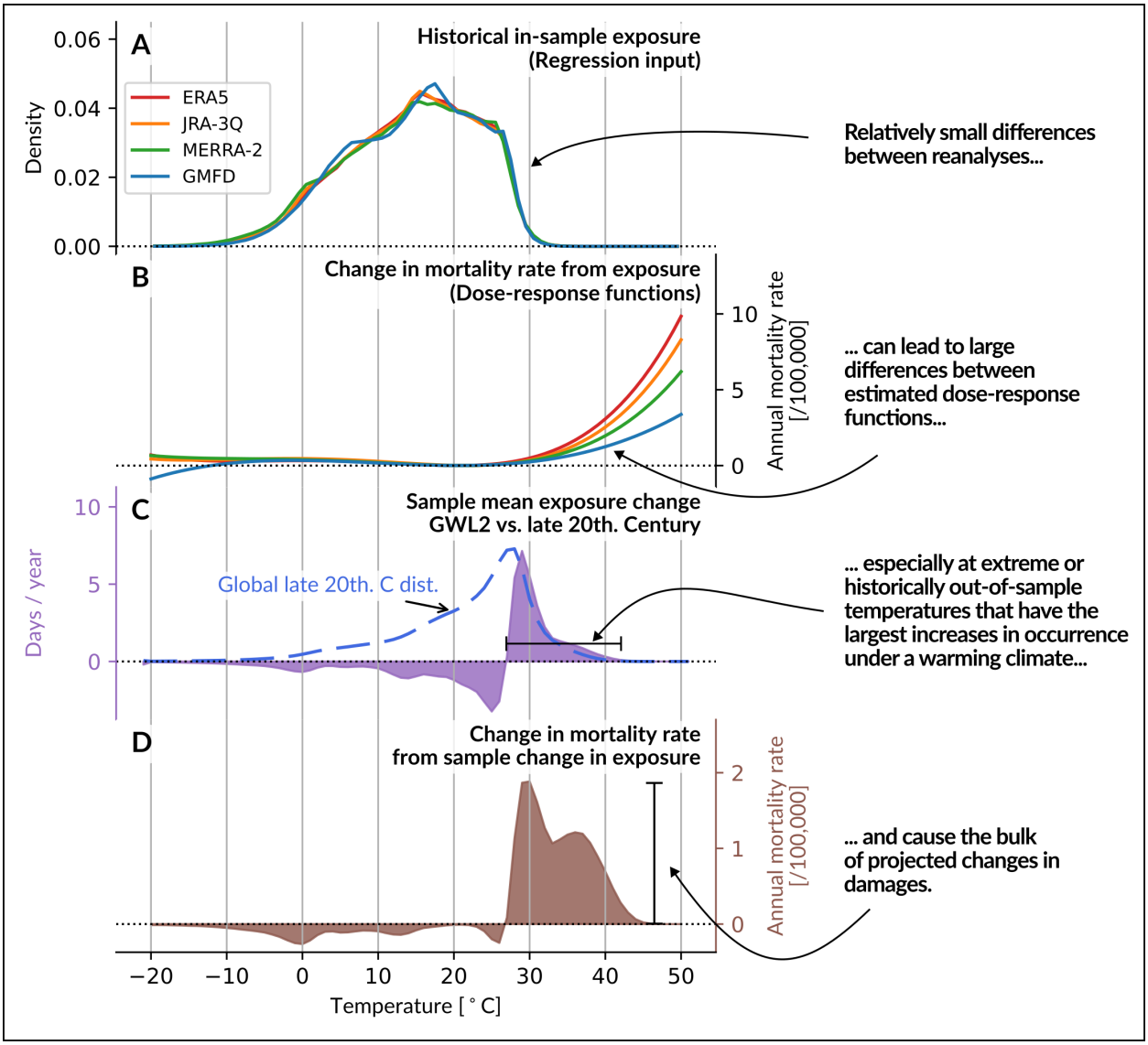


Fig. 1 Observational uncertainty and nonlinear impact amplification. (**A**) Exposure to daily temperature, fit using historical temperatures from four reanalyses (shown as population-weighted histograms over regions used in the fit). (**B**) Four dose-response curves for the quartic polynomial relationship between annual all-cause mortality rate and exposure to daily temperature. (**C**) Change in global population-weighted temperature between Global Warming Levels (GWLs) 0.61 (reflecting the late 20th century global climate) and 2 (representing a future world that has undergone additional climate change) for CanESM5, SSP2-4.5, r10i1p1f1, a randomly chosen future GCM projection, averaged across all four reanalysis bias-corrections. (**D**) Change in mortality rate for the same ensemble member associated with the change in temperature exposure in B, using the average of all four dose-response functions. All filled plots use 1-degree bins. Note that, since mortality data is only available for a subset of the globe, the historical in-sample climate in A is different from the baseline for B and C; the shape of the global

population-weighted temperature baseline distribution at GWL0.61 is shown in a dashed line (normalized to fit within the panel) in C for reference. See fig. S2 for a version showing only in-sample changes in temperature and mortality rate.

Crucially, due to the non-linearity common to climate-society relationships (*2*, *3*), even small differences in historical weather records can cause substantial differences in damage estimates when presented with extreme and out-of-sample future climate states that are expected to cause the bulk of changes in climate risks. For example, fitting a flexible quartic temperature-mortality model (*29*) on historical data from four different reanalysis products (Fig. 1A) produces four different dose-response curves (Fig. 1B). These curves may be well-constrained over commonly observed historic temperatures, but they diverge for the rare or wholly out-of-sample temperatures expected to see the largest increase in occurrence (Fig. 1C) and have the largest influence on changes in impacts (Fig. 1D). The mismatch between future exposure and historical support of the model is exacerbated if the training data (histograms in Fig. 1A) undersample those temperatures compared to the full global distribution (dashed line in Fig. 1C). Since the global distribution of exposure to temperature is strongly right-skewed (dashed line in Fig. 1C), even small shifts in the climate can expose substantial populations to these extreme or out-of-sample temperatures.

To test the importance of this uncertainty in estimates of historical weather conditions, we conduct a sensitivity analysis of climate impacts projections to all sources of climate uncertainty. We examine three dose-response functions from the statistical econometric climate impacts literature relating exposure to daily mean temperature to annual all-cause mortality (*29*) and national GDP per capita growth (*40*), and exposure to daily maximum temperature to annual payroll (*41*). These models span a broad range of common model configurations and decisions (see, e.g., fig. S1): different functional forms, different input variables, and different levels of spatial aggregation in input climate data. Among other characteristics, the mortality model represents state-of-the-art high-resolution nonlinear econometric climate impact modeling, the GDP per capita growth model is a highly-influential country-level global model, and the payroll model allows an exploration of the additional historical data products available to regional studies in data-rich areas.

We first re-estimate these impact models using four different commonly-used reanalysis products and use the resulting spread of estimates as a proxy for observational uncertainty in estimates of historical temperature exposure. We then use them to create projections of future damages, using projections of daily mean and maximum temperature from the "Bias-Corrected and Downscaled Massive Ensemble" (BCD-ME (*18*)) The BCD-ME accounts for scenario uncertainty by normalizing changes by Global Warming Levels (GWLs), samples internal variability and model uncertainty by collecting up to 86 runs each of 12 GCMs, and samples "reanalysis uncertainty", the spread across reanalysis products, by bias-correcting and downscaling separately against each of the same four reanalyses.

We show that over much of the globe, the future spread in these estimated climate impacts is dominated by the choice of reanalysis, primarily through its influence on the fitting of the original dose-response function, with a smaller role played by its influence on bias-correcting and downscaling future GCM output. Though the sign of the mean change in climate impacts is largely unaffected by the addition of estimates based on multiple historical gridded datasets, the total uncertainty in future damages, and thus also the risk of extreme damages, increases substantially.

Dose-response functions by reanalysis

We first refit historical relationships between mean daily temperature exposure and annual all-cause mortality (*29*), mean daily temperature exposure and GDP per capita growth (*40*), and maximum daily temperature exposure and payroll (*41*) using four reanalysis products as historical exposure: ERA5, MERRA-2, JRA-3Q, and GMFD (Fig. 2A, D, G). ERA5, MERRA-2, and JRA-3Q represent the three available global, continuously updating reanalysis products; GMFD is also commonly-used in impacts studies due to its role as the bias-correction and downscaling target for NASA's NEX-GDDP set of GCM projections.

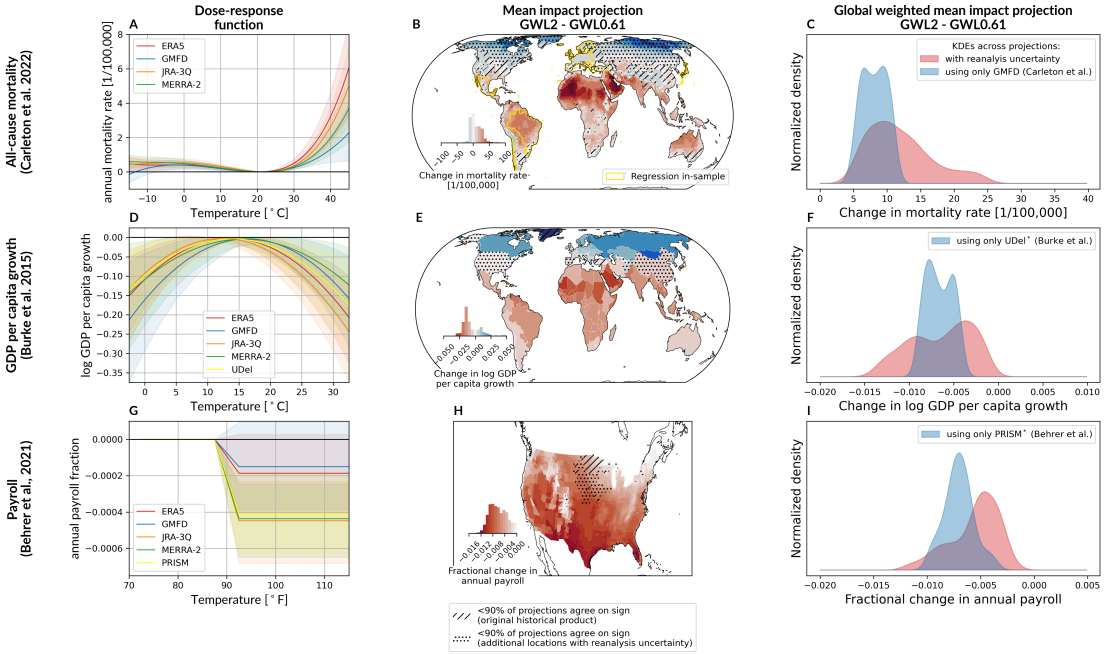


Fig. 2. Impact models and damage projections across reanalyses. (**A**), (**D**), (**G**) Dose-response functions fit on multiple reanalysis products. (**B**), (**E**), (**H**) Mean impact projections across BCD-ME runs and reanalyses from GWL0.61 to GWL2. Distribution across GCMs and runs of global (**C, F**) or CONUS (**I**) mean impact projections as normalized kernel density estimates across BCD-ME runs and reanalyses. Rows show mortality (A-C), GDP per capita growth (D-F), and payroll (G-I) impacts. In the left column, mortality and GDP per capita growth dose-response functions are plotted relative to their minimum between 0 and 25°C. The shading shows the 95% confidence interval across the statistical regression uncertainty; thick lines show the mean fit. Dose-response functions fit using UDel (in D) and PRISM (G) are included for reference; these were the original products used by each respective paper. In the middle column, hatching indicates regions where <95% of projections agree on signs when using the original product, dotted regions are the additional regions where this is the case when accounting for reanalysis uncertainty using our sample, in other words, where reanalysis uncertainty affects the robustness of the sign of the long-term change in climate impacts. In the right column, the distribution in blue show the range of projected impacts when only using the product from each dose-response function's original paper (see supplementary materials for details). Yellow borders in (B) show the regions with input data included in the mortality regression.

The dose-response functions for mortality agree among the reanalyses between 0°C and 25°C (Fig. 2A, the well-sampled range of historical temperatures as shown in Fig. 1), but diverge strongly at colder and hotter temperatures. The dose-response functions also diverge at the extremes in the GDP per capita growth model of Burke et al. (*40*) (Fig. 2D). Using MERRA-2 and GMFD, the 'ideal' temperature that maximizes GDP per capita growth, i.e., the vertex in the quadratic model, is 3-4°C warmer than for ERA5 and JRA-3Q, and extreme heat is associated with lower damages.

For projections of payroll in the continental United States, fit on daily maximum instead of mean temperature, we find that GMFD estimates the least (and statistically insignificant) damages from an extra day above 90° F, and MERRA-2 the most. Note that the spread across reanalyses encompasses the dose-response functions fit on UDel (GDP per capita growth) and PRISM (payroll), the statistically interpolated weather products used by the original studies (Fig. 2D, G).

In short, the choice of observational dataset has a substantial impact on the climate impact model fit. The relative ordering of gridded historical data product differs between impact models; though for both polynomial dose-response functions based on mean daily temperature, ERA5 and JRA-3Q predict higher damages at higher temperatures, while GMFD and MERRA-2 predict lower damages. Thus, the relationship between the choice of data product and the resultant climate impact model may depend on both the functional form of the impact model and the underlying climate metric.

Reanalysis models have different native resolutions; however, this is not the primary cause of differences between dose-response functions (fig. S3D-F). Reanalyses span different years, with GMFD data in particular ending in 2010 (for mean temperature) or 2008 (for maximum temperature). Again, these results are robust when fitting each model over all years with data for a given reanalysis (fig. S3J-L).

Partitioning uncertainty in damages

We estimate future damages associated with each dose-response function using bias-corrected and downscaled climate model projections with the same reanalysis product from the BCD-ME (see supplementary material). On average, our damage projections resemble those of their original papers with higher mortality and lower GDP per capita growth in the tropics, the converse in the high latitudes, a transition zone in the mid-latitudes, and higher payroll damages in the southern United States (Fig. 2 middle column).

Accounting for the spread across reanalyses substantially increases the likely range of projected damages (Fig. 2 right column), with the 95% percentile across projections increasing in magnitude by 104%, 42%, and 6% and the 5-95% range increasing by roughly 3.0, 2.6, and 1.5 for mortality, GDP per capita growth, and payroll changes, respectively, when compared to projections using only the historical gridded data product from each original study. The sign of the change in impacts is largely unaffected (see Fig. 2, middle column).

Our focus is on the sources of climate uncertainty driving the spread in these projections rather than the mean impact itself. We partition this spread into contributions from regression uncertainty and climate uncertainty, finding that climate uncertainty is larger for the majority of the globe (by area or population) for mortality and payroll projections, and is larger for nearly half of the globe for GDP per capita growth (fig. S4). We then partition the spread of climate uncertainty into contributions from model uncertainty, internal variability, and reanalysis choice. Using impacts projections driven by future climate states from up to 334 runs from 12 GCMs allows a representative sampling of the magnitude of internal variability (fig. S5) and model uncertainty (fig. S6); comparing projections using dose-response functions and bias-correction and downscaling procedures from four reanalyses gives an estimate of the uncertainty across commonly-used historical data products.

Uncertainty in damages are dominated by the spread across reanalyses, termed “reanalysis uncertainty”, a proxy for the true observational uncertainty in estimates of the past climate (Fig.

3). That is, the choice of historical product is the most important source of climate uncertainty for most of the globe for changes at GWL2 (93%, 86%, and 98% of locations by area for mortality, GDP per capita growth, and payroll, respectively, or 78%, 78%, and 96% of locations by population), particularly in the mid-latitudes, with model uncertainty still making up the majority of the spread in large parts of the tropics.

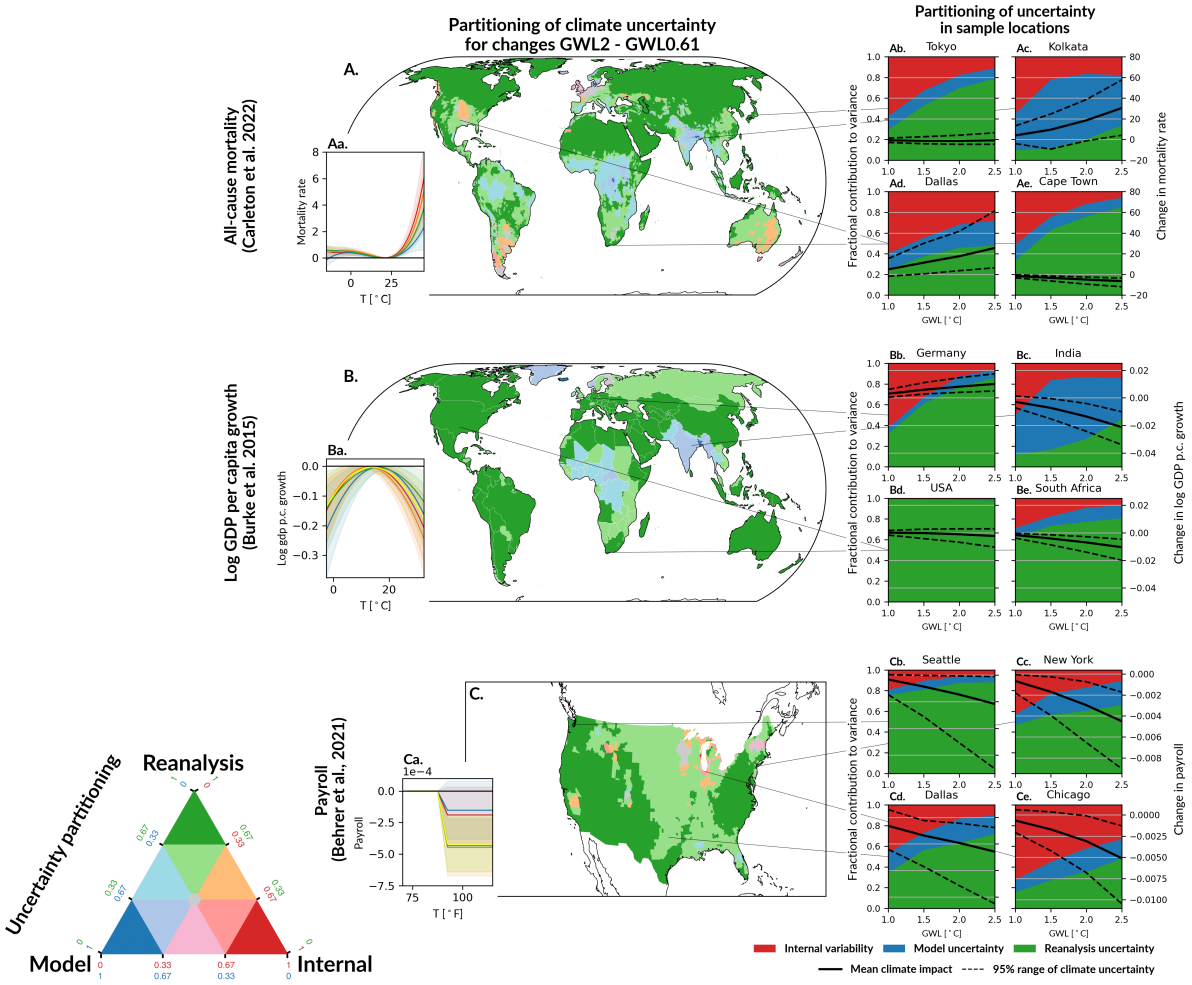


Fig. 3. Partitioning of climate uncertainty by impact. Partitioning of climate uncertainty for projections of the impact of climate change on mortality (**A-Ae**), GDP per capita growth (**B-Be**), and payroll (**C-Ce**). Uncertainty is calculated as the variance across changes between GWL 0.61 (1982-2001) and GWL 2 for each metric. Maps (A, B, C) are colored by the dominant source of climate uncertainty, with primary colors representing areas where reanalysis (green), model (blue), or internal (red) uncertainty makes up more than 2/3 of the spread and lighter colors representing areas with a mix of uncertainty sources (see triangular color legend at bottom left). The panels on the right-hand side show the evolution of the partitioning of uncertainty over different GWLs for select representative locations in addition to the evolution over time of mean damages across the ensemble (solid black line) and the 95-percentile spread across sources of climate uncertainty (i.e., the spread across model uncertainty, internal variability, and reanalysis uncertainty; shown as dashed lines). Panels (Aa), (Ba), and (Ca) show the damage functions from Fig. 2 for reference.

Reanalysis uncertainty dominates the global spread of impacts for changes across all GWLs studied, though the relative mix of uncertainty sources may vary -- as has been found elsewhere (*15*, *17*, *42*). For example, internal variability tends to have a somewhat constant magnitude across lead times and thus contributes a larger percentage of total variance at shorter lead times (with smaller changes), with model uncertainty increasing its share of total uncertainty at higher

GWLs (Fig. 3 right panels and Figs. S6 and S9). In line with Schwarzwald et al. (*17*), internal variability can contribute a similar or larger magnitude as the spread across GCMs to total climate uncertainty over large swaths of the mid-latitudes through GWL2 (fig. S10).

For changes by year instead of by GWL, model uncertainty is boosted due to differences in climate sensitivities between models, but reanalysis uncertainty is still the largest source of climate uncertainty for most of the globe for all but the shortest lead times (figs. S8, S11, and supplementary methods).

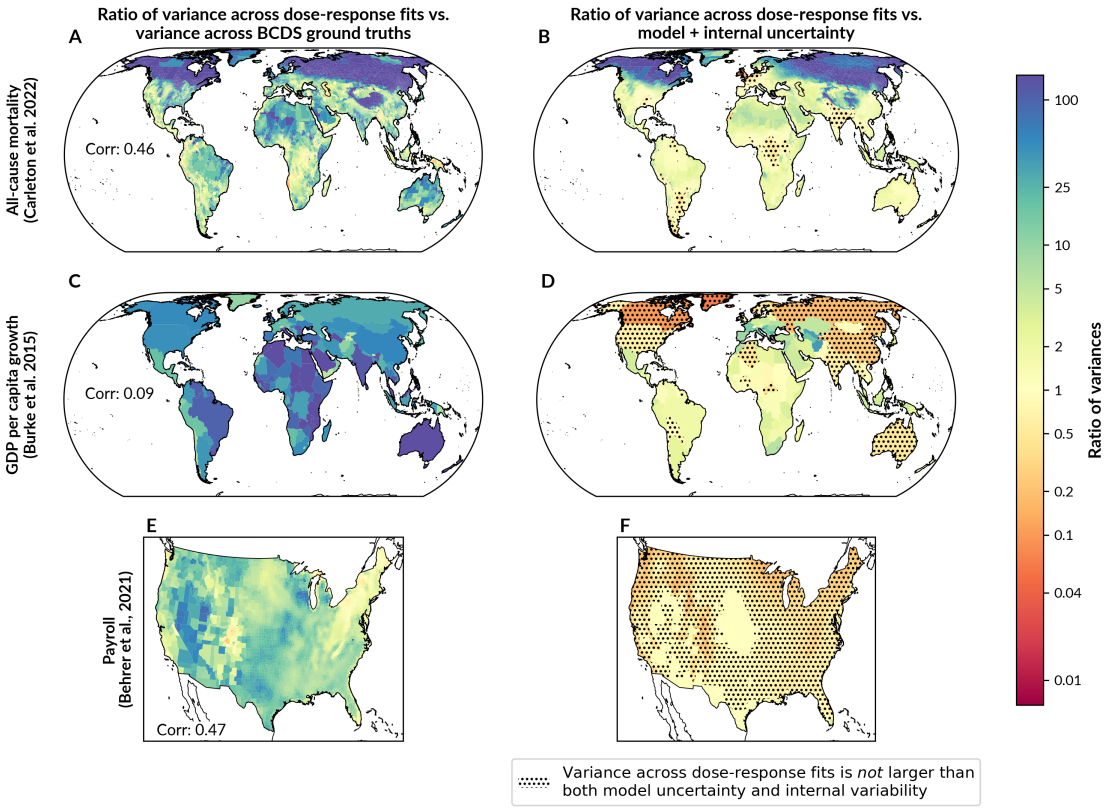


Fig. 4. Drivers of reanalysis uncertainty. Relative importance of different pathways of reanalysis uncertainty in projections of climate impacts between GWL0.61 and GWL 2. For each impact, the left column shows the ratio of the relative contributions to reanalysis uncertainty of the dose-response function pathway vs. the bias-correction and downscaling pathway and the right column shows the ratio of the magnitude of uncertainty through only the dose-response function pathway to the sum of variances from model uncertainty and internal variability (see supplementary materials for details). In the left column, Pearson's correlation coefficients (across locations, in log space) between variances in the dose-response fit and bias-correction and downscaling pathways are printed. In the right column, lack of hatching means that the spread across dose-response functions alone is the largest single contributor to climate uncertainty.

Pathways of observational uncertainty

Since the choice of reanalysis influences impact projections in two ways, we divide the total reanalysis uncertainty into contributions from fitting dose-response functions and from bias-correcting and downscaling (Fig. 4, see supplementary materials for details). Uncertainty associated with fitting the dose-response functions dominates for most parts of the world (greenish-to-bluish regions in Fig. 4, left column). In fact, for mortality, the spread across dose-response functions by itself is larger than the sum of variances due to model uncertainty and

internal variability for most of the globe (for GDP per capita growth, this is the case for nearly half of the globe by population).

For mortality and payroll projections, the variances in these two sources are spatially correlated, for the GDP per capita growth model, they are not (correlations in the left column of Fig. 4). Whether this is the case depends on how similar reanalysis uncertainty is in the parts of the temperature distribution that most affect the dose-response fits vs. in the parts of the distribution that most drive future damages and thus depends on a complex interplay between the functional form of the impact function, historical exposure, and the bias-correction and downscaling procedure.

Discussion

In climate impacts studies, the choice of gridded weather record used to fit relationships between climate and society and to post-process GCM output has often been either *ad hoc* or done for reasons unrelated to a product's suitability to accurately represent the desired climate metrics in the regions of study. We have shown that this choice interacts with the functional form of the climate impact and other impact modeling decisions to introduce implicit uncertainty in projections of future climate damages of a magnitude greater than the spread across different GCMs in many parts of the world. In other words, the most important source of climate uncertainty in projections of climate impacts may be the choice of historical data product.

Since this observational uncertainty is not commonly addressed, uncertainties in future damages are likely underestimated, resulting in underestimations of the Social Cost of Carbon (*12*, *13*) and possible overlooking of plausible but extreme tail risks; we show, for example, that the 95th percentile across all projections increases in magnitude by 104%, 43%, and 6% for mortality, GDP per capita growth, and annual payroll, respectively, when accounting for reanalysis uncertainty (though we note that changes in the sign of the signal are rare).

Uncertainty in observational datasets interacts with the modeling of climate impacts in complex ways (fig. S1); our sample of impacts functions and reanalyses allows us to analyze a subset of these pathways. We show that the partitioning of uncertainty depends not only on region and lead time, but also on the climate variable used and, crucially, the functional form of the dose-response model, with the Behrer et al. (*41*) payroll model, based on threshold exceedances of maximum daily temperature, producing a different clustering of gridded historical data products than the polynomial, mean temperature-driven models of Carleton et al. (*29*) and Burke et al. (*40*). More flexible functional forms (such as polynomial-based dose-response functions) are particularly susceptible to reanalysis uncertainty, especially when coupled with other aspects of impact models that interact with the choice of historical gridded weather product (fig. S1, see also supplementary material on differences between the Carleton et al. ‘pooled’ and ‘interacted’ specifications and fig. S15 for more details).

In this study, we primarily use differences between reanalysis datasets as a proxy for the observational uncertainty due to imperfect estimates of the past climate, since these datasets span many of the commonly-used weather records in climate impacts studies. Reanalyses differ in which data sources (satellites, weather stations, etc.) they assimilate, how they characterize sub-grid processes, and their resolutions. We find resolution is unlikely to explain the uncertainty in projected damages. We calculate reanalysis uncertainty under flat priors across reanalyses, which is in line with how these products are used in practice and may be unavoidable if evaluations do

not exist for a metric or region of interest. However, this assumption almost certainly underestimates the true observational uncertainty as the products used in this study share imperfect observations and model assumptions. None of the reanalyses studied here were consistent outliers in their impact on our estimate of reanalysis uncertainty; in fact, all four reanalyses were the largest contributor to this uncertainty for at least some impacts and locations in our sample (supplementary materials and fig. S16).

A reader may reasonably ask if the gridded historical climate data products analyzed here are fully representative of the possible data sources for climate impact studies. For global studies requiring high-resolution daily data across data-spare regions, reanalyses, which are based on physical weather models, make up the bulk of currently published products. The reanalyses studied here span most commonly-used products while omitting legacy products such as JRA-55 and ERA-Interim. Statistically interpolated or blended global daily products either depend on reanalyses for daily-scale variability (such as the Climate Hazard Group's CHIRTS, which uses ERA5 for this purpose (*43*)) or statistically infill using station records with limited coverage in many regions of the world.

Global studies requiring mean temperature at monthly or lower temporal frequency have similarly limited high-resolution data options; Berkeley Earth (*44*) may be the only additional suitable product. Users should exercise caution when selecting globally complete datasets; some, such as CRU-TS, replace values with a location's climatological mean when sufficient observations are not available (*45*) and therefore cannot be treated as statistically complete. Regional studies in areas with high observational density can sometimes take advantage of a greater variety of products. In North America, for example, additional products range from purely statistical interpolation of weather station output (such as nClimGrid (*46*)), to terrain-informed interpolations (such as Daymet (*47*) or PRISM (*48*)), to blended products that also assimilate satellite records, to regionally-specific reanalyses (such as NLDAS (*49*)).

To compare our reanalysis-based results to these other datasets, we fit the GDP per capita growth model using Berkeley Earth monthly temperature and the payroll model using four additional regional products specific to North America (fig. S11). The former falls within the range of the reanalyses products. In the latter case, these additional data result in a similar spread in dose-response functions as the reanalyses, though with a somewhat larger damage estimate for the same maximum daily temperatures. In the absence of strong priors about the relative suitability of a particular subset of these additional data products, our overall conclusion, of the importance of observational uncertainty, remains.

In this study, we intentionally focus on a single lever to illustrate our point about observational climate uncertainty–differences in temperature records alone. Though all impact models analyzed here include annual precipitation as controls, none depend much on the choice of precipitation product (fig. S12), though the regression coefficients on the precipitation variables are indeed highly sensitive to the input product (Tables S1-S3). We note, however, that though characteristics of variables such as precipitation (e.g., smaller characteristic spatial scale, lower model skill, etc.) may result in greater observational uncertainty, generalizing a resultant partitioning of uncertainty in projections of climate risks based on those variables is difficult: variables harder to model in reanalyses are also harder to do so in GCMs, possibly resulting in greater model uncertainty, and hydrological variables in particular tend to be strongly influenced by internal variability (*42*, *50*).

Previous work has begun to disentangle the causes of differences between gridded historical data products. For example, MERRA-2 has a known too-wet soil-moisture bias, affecting precipitation and temperature near the surface (*51–53*) and possibly explaining the substantially different 'ideal' temperatures for GDP growth predicted by the product. Future extensions of such work could evaluate not only the geographic regions where differences between gridded historical data products are most likely to affect climate impact models, but also what parts of the distribution are driving these differences, to highlight priorities for constraining uncertainties.

We show an example of such an analysis in fig. S13, focusing on the GDP per capita growth model that, with its balanced panel of countries, is the simplest to diagnose in our sample of dose-response functions. We refit the model using a leave-one-out analysis by country. The spread between dose-response functions fit using different reanalyses generally increases when including tropical, poorer countries in the sample (fig. S13A, D, E), in line with well-known biases of climate observational network densities towards richer countries in the Global North (*20–22*). Two additional failure modes are highlighted: Rwanda, where differences between reanalyses increase dramatically during the Rwandan Civil War and Genocide and take more than a decade to recover, in line with the conflict's disruption to the local meteorological network (*20*), and Cabo Verde, where an error in the GMFD ocean fields creates a spurious signal in 2007 and 2008 (fig. S13B, C).

We emphasize that the 'observational' reanalysis uncertainty highlighted in this paper is epistemologically different from other sources of climate uncertainty in that gridded historical data products are estimates of the actual realized climate at every location and metric of interest. They are, however, necessarily imperfect due to incomplete and biased observations. Evaluations to identify best-performing products exist for certain parts of the world, though this exercise is non-trivial: apart from the challenges of evaluating area-averaged gridded variables using point sources, 'ground truth' in-situ observations contain systemic biases themselves, are rare in regions likely to experience the worst effects of climate change, and extant verification datasets are often not independent from the gridded weather records (*19–23*). All evaluations are not equally useful, especially if they do not cover the features of climate distributions most relevant to projections of climate impacts. Simple climate impact models such as the ones studied here can serve as a filter to highlight where tail behavior has the largest consequences for projections, though in doing so, they may hint at a fundamental limit to constraining observational uncertainty in future projections. As we have shown, for particularly flexible functional forms, climate impact model behavior is most poorly constrained in the out-of-sample temperature range expected to cause the largest change in damages.

We also note that we focus here on the quantifiable, implicit, and inherent uncertainty that stems from the use of climate data in projections of climate impacts and is realized through the spread across or within GCMs and across reanalyses. The credibility of this range depends on reanalysis skill in replicating the historical climate and GCM skill in modeling the real climate, respectively (and, additionally, how well GCMs replicate the real-world relationship between GWLs and local temperatures). In some regions with particularly poor in-situ weather measurements or in areas with known systemic biases in GCMs, users of climate and climate impact projections in risk contexts may be limited by the constraints of what is currently able to be modelled.

We conclude with three sets of recommendations. First, we urge impact modelers to test the sensitivity of their results with a variety of latest-generation gridded historical weather data records, especially if no evaluation of these products exists for variables of interest in the regions of study. It is also crucial to consider how the choice of functional form may cause the range of

out-of-sample impacts to be more or less constrained, especially given the reality that 'perfect' historical climate observations are unattainable.

Second, we call for research into better constraining historical observational uncertainty, though we recognize that this may not be feasible in all cases (barring data rescue operations, the density of the historical observational network in the past is fixed, for example). An impacts-informed approach to studying observational uncertainty, using dose-response functions from the literature as done in this paper, can help highlight at what parts of the distribution of climate variables and in what regions of the world discrepancies between observational data products are most likely to affect projections of climate impacts, and thus help target improvements in these products.

Finally, our results suggest that an auditor of future climate impact projections, be it in academia or elsewhere, may not only wish to ascertain that projections capture the well-known uncertainty from models and internal variability, but also demand to know which estimate of the historical climate they assume to be the 'ground truth'.

Climate projections from ensembles of GCMs and estimates of climate risks using those projections concretely influence decision-making, through for example their role in financial risk modeling or in cost-benefit analyses through estimates of the Social Cost of Carbon. Good decisions need good data; as has been shown in the literature on climate forecasting, for example, the value of accurate information about future climate states is substantial (*54*), as are the costs when access to that information is limited or unequal (*55*). On longer timescales, we have shown here that uncertainty in projections of climate impacts is strongly affected not just by the spread across GCMs or modeling decisions underlying estimates of climate-society relationships, but also by imperfect historical estimates of the true weather, whose uncertainty is higher in poorer, hotter countries. Considering and constraining this uncertainty is therefore crucial to supporting decisions in climate adaptation and mitigation contexts and to painting an accurate picture of the tail risks of climate change.

References and Notes

1. J. Rising, M. Tedesco, F. Piontek, D. A. Stainforth, The missing risks of climate change. *Nature* **610**, 643–651 (2022).

2. M. Auffhammer, S. M. Hsiang, W. Schlenker, A. Sobel, Using Weather Data and Climate Model Output in Economic Analyses of Climate Change. *Rev. Environ. Econ. Policy* **7**, 181–198 (2013).

3. T. A. Carleton, S. M. Hsiang, Social and economic impacts of climate. *Science* **353**, aad9837 (2016).

4. S. Hsiang, R. Kopp, A. Jina, J. Rising, M. Delgado, S. Mohan, D. J. Rasmussen, R. Muir-Wood, P. Wilson, M. Oppenheimer, K. Larsen, T. Houser, Estimating economic damage from climate change in the United States. *Science* **356**, 1362–1369 (2017).

5. D. Lemoine, C. Hausman, J. G. Shrader, Navigating the "Problem from Hell": A Guide to Climate Damages. *J. Econ. Lit.*, doi: 10.1257/jel.20261773 (in print).

6. S. Hsiang, The Global Economic Impact of Climate Change: An Empirical Perspective. doi: 10.1146/annurev-economics-102224-021145 (2026).

7. M. Condon, Climate Services: The Business of Physical Risk. *Ariz. State Law J.* **55**, 147–210 (2023).

8. J. E. Aldy, M. J. Kotchen, R. N. Stavins, J. H. Stock, Keep climate policy focused on the social cost of carbon. *Science* **373**, 850–852 (2021).

9. G. Wagner, D. Anthoff, M. Cropper, S. Dietz, K. T. Gillingham, B. Groom, J. P. Kelleher, F. C. Moore, J. H. Stock, Eight priorities for calculating the social cost of carbon. *Nature* **590**, 548–550 (2021).

10. K. Rennert, F. Errickson, B. C. Prest, L. Rennels, R. G. Newell, W. Pizer, C. Kingdon, J. Wingenroth, R. Cooke, B. Parthum, D. Smith, K. Cromar, D. Diaz, F. C. Moore, U. K. Müller, R. J. Plevin, A. E. Raftery, H. Ševčíková, H. Sheets, J. H. Stock, T. Tan, M. Watson, T. E. Wong, D. Anthoff, Comprehensive evidence implies a higher social cost of CO2. *Nature* **610**, 687–692 (2022).

11. F. C. Moore, M. A. Drupp, J. Rising, S. Dietz, I. Rudik, G. Wagner, Synthesis of evidence yields high social cost of carbon due to structural model variation and uncertainties. *Proc. Natl. Acad. Sci.* **121**, e2410733121 (2024).

12. C. Proistosescu, G. Wagner, Uncertainties in Climate and Weather Extremes Increase the Cost of Carbon. *One Earth* **2**, 515–517 (2020).

13. D. Lemoine, The Climate Risk Premium: How Uncertainty Affects the Social Cost of Carbon. *J. Assoc. Environ. Resour. Econ.* **8**, 27–57 (2021).

14. S. Hallegatte, Strategies to adapt to an uncertain climate change. *Glob. Environ. Change* **19**, 240–247 (2009).

15. E. Hawkins, R. Sutton, The Potential to Narrow Uncertainty in Regional Climate Predictions. *Bull. Am. Meteorol. Soc.* **90**, 1095–1108 (2009).

16. M. Burke, J. Dykema, D. B. Lobell, E. Miguel, S. Satyanath, Incorporating Climate Uncertainty into Estimates of Climate Change Impacts. *Rev. Econ. Stat.* **97**, 461–471 (2014).

17. K. Schwarzwald, N. Lenssen, The importance of internal climate variability in climate impact projections. *Proc. Natl. Acad. Sci.* **119**, e2208095119 (2022).

18. K. Schwarzwald, N. Lenssen, R. M. Horton, G. Wagner, A bias-corrected & downscaled massive ensemble to diagnose uncertainty in climate impact projections. *Sci. Data*, doi: 10.1038/s41597-026-08391-w (2026).

19. S. Heft-Neal, D. B. Lobell, M. Burke, Using remotely sensed temperature to estimate climate response functions. *Environ. Res. Lett.* **12**, 014013 (2017).

20. T. Dinku, Overcoming challenges in the availability and use of climate data in Africa. *ICT Update* (2018).

21. T. Dinku, "Challenges with availability and quality of climate data in Africa" in *Extreme Hydrology and Climate Variability*, A. M. Melesse, W. Abtew, G. Senay, Eds. (Elsevier, 2019; http://www.sciencedirect.com/science/article/pii/B9780128159989000075), pp. 71–80.

22. J. Su, C. Miao, F. Zwiers, H. Beck, P. Jones, Q. Sun, L. J. Slater, W. R. Berghuijs, Y. Wada, D. Rosenfeld, J. Gou, Y. Wu, P. Tarolli, P. Borrelli, P. Panagos, L. V. Alexander, Q. Zhang, J. Hu, S.-K. Min, L. Samaniego, Q. Duan, G. Destouni, J. A. Marengo, R. Modarres, S. Sorooshian, Precipitation observing network gaps limit climate change impact assessment. *Nature* **652**, 119–125 (2026).

23. D. Hogan, W. Schlenker, Non-linear relationships between daily temperature extremes and US agricultural yields uncovered by global gridded meteorological datasets. *Nat. Commun.* **15**, 4638 (2024).

24. I. Muhire, F. Ahmed, Spatiotemporal trends in mean temperatures and aridity index over Rwanda. *Theor. Appl. Climatol.* **123**, 399–414 (2016).

25. H. Hersbach, B. Bell, P. Berrisford, S. Hirahara, A. Horányi, J. Muñoz Sabater, J. Nicolas, C. Peubey, R. Radu, D. Schepers, A. Simmons, C. Soci, S. Abdalla, X. Abellan, G. Balsamo, P. Bechtold, G. Biavati, J. Bidlot, M. Bonavita, G. D. Chiara, P. Dahlgren, D. Dee, M. Diamantakis, R. Dragani, J. Flemming, R. Forbes, M. Fuentes, A. Geer, L. Haimberger, S. Healy, R. J. Hogan, E. Hólm, M. Janisková, S. Keeley, P. Laloyaux,

P. Lopez, C. Lupu, G. Radnoti, P. de Rosnay, I. Rozum, F. Vamborg, S. Villaume, J.-N. Thépaut, The ERA5 global reanalysis. *Q. J. R. Meteorol. Soc.* **146**, 1999–2049 (2020).

26. M. G. Bosilovich, S. Akella, L. Coy, R. Cullather, C. Draper, R. Gelaro, R. Kovach, Q. Liu, A. Molod, P. Norris, K. Wargan, W. Chao, R. Reichle, L. Takasc, Y. Vikhliaev, S. Bloom, A. Collow, S. Firth, G. Labow, G. Partyka, S. Pawson, O. Reale, S. D. Schubert, M. Suarez, "MERRA-2: Initial Evaluation of the Climate" (NASA/TM-2015-104606/Vol.43, NASA, 2015); https://gmao.gsfc.nasa.gov/pubs/docs/Bosilovich803.pdf.

27. Y. Kosaka, S. Kobayashi, Y. Harada, C. Kobayashi, H. Naoe, K. Yoshimoto, M. Harada, N. Goto, J. Chiba, K. Miyaoka, R. Sekiguchi, M. Deushi, H. Kamahori, T. Nakaegawa, T. Y. Tanaka, T. Tokuhiro, Y. Sato, Y. Matsushita, K. Onogi, The JRA-3Q Reanalysis. *J. Meteorol. Soc. Jpn. Ser II* **102**, 49–109 (2024).

28. J. Sheffield, G. Goteti, E. F. Wood, Development of a 50-Year High-Resolution Global Dataset of Meteorological Forcings for Land Surface Modeling. *J. Clim.* **19**, 3088–3111 (2006).

29. T. Carleton, A. Jina, M. Delgado, M. Greenstone, T. Houser, S. Hsiang, A. Hultgren, R. E. Kopp, K. E. McCusker, I. Nath, J. Rising, A. Rode, H. K. Seo, A. Viaene, J. Yuan, A. T. Zhang, Valuing the Global Mortality Consequences of Climate Change Accounting for Adaptation Costs and Benefits*. *Q. J. Econ.* **137**, 2037–2105 (2022).

30. A. Rode, T. Carleton, M. Delgado, M. Greenstone, T. Houser, S. Hsiang, A. Hultgren, A. Jina, R. E. Kopp, K. E. McCusker, I. Nath, J. Rising, J. Yuan, Estimating a social cost of carbon for global energy consumption. *Nature* **598**, 308–314 (2021).

31. A. Hultgren, T. Carleton, M. Delgado, D. R. Gergel, M. Greenstone, T. Houser, S. Hsiang, A. Jina, R. E. Kopp, S. B. Malevich, K. E. McCusker, T. Mayer, I. Nath, J. Rising, A. Rode, J. Yuan, Impacts of climate change on global agriculture accounting for adaptation. *Nature* **642**, 644–652 (2025).

32. National Center for Atmospheric Research Staff, "The Climate Data Guide: NCEP-NCAR (R1): An Overview." (UCAR, 2025); https://climatedataguide.ucar.edu/climate-data/ncep-ncar-r1-overview.

33. B. Thrasher, W. Wang, A. Michaelis, F. Melton, T. Lee, R. Nemani, NASA Global Daily Downscaled Projections, CMIP6. *Sci. Data* **9**, 262 (2022).

34. L. Huang, X. Fang, T. Zhang, H. Wang, L. Cui, L. Liu, Evaluation of surface temperature and pressure derived from MERRA-2 and ERA5 reanalysis datasets and their applications in hourly GNSS precipitable water vapor retrieval over China. *Geod. Geodyn.* **14**, 111–120 (2023).

35. R. Bodjrenou, J.-M. Cohard, B. Hector, E. A. Lawin, G. Chagnaud, D. K. Danso, Y. N. M'po, F. Badou, B. Ahamide, Evaluation of Reanalysis Estimates of Precipitation, Radiation, and Temperature over Benin (West Africa). *J. Appl. Meteorol. Climatol.* **62**, 1005–1022 (2023).

36. J. D. Keller, S. Wahl, Representation of Climate in Reanalyses: An Intercomparison for Europe and North America. *J. Clim.* **34**, 1667–1684 (2021).

37. M. Taszarek, N. Pilguj, J. T. Allen, V. Gensini, H. E. Brooks, P. Szuster, Comparison of Convective Parameters Derived from ERA5 and MERRA-2 with Rawinsonde Data over Europe and North America. *J. Clim.* **34**, 3211–3237 (2021).

38. B. El Kihel, N. E. El Kadri Elyamani, A. Chillali, Evaluation of wind potential and economic prospects in the southern regions of Morocco with MERRA-2 and ERA5. *Wind Eng.* **49**, 475–498 (2025).

39. Y. Yang, Q. Li, Z. Song, W. Sun, W. Dong, A comparison of global surface temperature variability, extremes and warming trend using reanalysis datasets and CMST-Interim. *Int. J. Climatol.* **42**, 5609–5628 (2022).

40. M. Burke, S. M. Hsiang, E. Miguel, Global non-linear effect of temperature on economic production. *Nature* **527**, 235–239 (2015).

41. A. P. Behrer, R. J. Park, G. Wagner, C. M. Golja, D. W. Keith, Heat has larger impacts on labor in poorer areas*. *Environ. Res. Commun.* **3**, 095001 (2021).

42. F. Lehner, C. Deser, N. Maher, J. Marotzke, E. M. Fischer, L. Brunner, R. Knutti, E. Hawkins, Partitioning climate projection uncertainty with multiple large ensembles and CMIP5/6. *Earth Syst. Dyn.* **11**, 491–508 (2020).

43. A. Verdin, C. Funk, P. Peterson, M. Landsfeld, C. Tuholske, K. Grace, Development and validation of the CHIRTS-daily quasi-global high-resolution daily temperature data set. *Sci. Data* **7**, 303 (2020).

44. R. A. Rohde, Z. Hausfather, The Berkeley Earth Land/Ocean Temperature Record. *Earth Syst. Sci. Data* **12**, 3469–3479 (2020).

45. I. Harris, T. J. Osborn, P. Jones, D. Lister, Version 4 of the CRU TS monthly high-resolution gridded multivariate climate dataset. *Sci. Data* **7**, 109 (2020).

46. I. Durre, A. Arguez, C. J. Schreck, M. F. Squires, R. S. Vose, Daily High-Resolution Temperature and Precipitation Fields for the Contiguous United States from 1951 to Present. *J. Atmos. Ocean. Technol.* **39**, 1837–1855 (2022).

47. P. E. Thornton, R. Shrestha, M. Thornton, S.-C. Kao, Y. Wei, B. E. Wilson, Gridded daily weather data for North America with comprehensive uncertainty quantification. *Sci. Data* **8**, 190 (2021).

48. C. Daly, M. Halbleib, J. I. Smith, W. P. Gibson, M. K. Doggett, G. H. Taylor, J. Curtis, P. P. Pasteris, Physiographically sensitive mapping of climatological temperature and precipitation across the conterminous United States. *Int. J. Climatol.* **28**, 2031–2064 (2008).

49. Y. Xia, K. Mitchell, M. Ek, J. Sheffield, B. Cosgrove, E. Wood, L. Luo, C. Alonge, H. Wei, J. Meng, B. Livneh, D. Lettenmaier, V. Koren, Q. Duan, K. Mo, Y. Fan, D. Mocko, Continental scale water and energy flux analysis and validation for the North American Land Data Assimilation System project phase 2 (NLDAS 2): 1. Intercomparison and application of model products. *J. Geophys. Res. Atmos.* **117**, 2011JD016048 (2012).

50. K. Schwarzwald, N. Lenssen, "Sources of uncertainty in climate model ensembles" in *Reference Module in Earth Systems and Environmental Sciences* (Elsevier, 2026; https://www.sciencedirect.com/science/article/pii/B9780443157486001027).

51. M. Hirschi, P. Stradiotti, B. Crezee, W. Dorigo, S. I. Seneviratne, Potential of long-term satellite observations and reanalysis products for characterising soil drying: trends and drought events. *Hydrol. Earth Syst. Sci.* **29**, 397–425 (2025).

52. B. Tian, E. J. Fetzer, J. Teixeira, Assessing the Tropospheric Temperature and Humidity Simulations in CMIP3/5/6 Models Using the AIRS Obs4MIPs V2.1 Data. *J. Geophys. Res. Atmos.* **129**, e2023JD040536 (2024).

53. C. Draper, R. H. Reichle, Assimilation of Satellite Soil Moisture for Improved Atmospheric Reanalyses. *Mon. Weather Rev.* **147**, 2163–2188 (2019).

54. H. Farkas, M. Linsenmeier, M. Talevi, P. Avner, B. Arga Jafina, M. Sidibe, "The Economic Value of Weather Forecasts: A Quantitative Systematic Literature Review" (Policy Research Working Paper 11213, World Bank, Washington, DC, 2025); https://doi.org/10.1596/1813-9450-11213.

55. M. Linsenmeier, J. Shrader, Global inequalities in weather forecasts. [Preprint] (2025). https://jeffreyshrader.com/papers/Linsenmeier%20Shrader%20-%20Global%20Forecast%20Inequality.pdf.

56. BCD-ME 1° bias-corrected (QDM) temperature time series, Earthmover Data Marketplace (2026); https://doi.org/https://doi.org/10.82924/9p8f-hd64.

57. BCD-ME 0.25° bias-corrected (QDM) and downscaled temperature statistics, Earthmover Data Marketplace (2026); https://doi.org/https://doi.org/10.82924/k92n-qb44.

58. R. P. Abernathey, T. Augspurger, A. Banihirwe, C. C. Blackmon-Luca, T. J. Crone, C. L. Gentemann, J. J. Hamman, N. Henderson, C. Lepore, T. A. McCaie, N. H. Robinson, R. P. Signell, Cloud-Native Repositories for Big Scientific Data. *Comput. Sci. Eng.* **23**, 26–35 (2021).

59. W. Schlenker, Daily Weather Data - Continental USA, version 2018, Zenodo (2024); https://doi.org/10.5281/ZENODO.10625287.

60. J. Wang, N. Nikolaou, M. an der Heiden, C. Irrgang, High-resolution modeling and projection of heat-related mortality in Germany under climate change. *Commun. Med.* **4**, 206 (2024).

61. C. W. Callahan, J. S. Mankin, Globally unequal effect of extreme heat on economic growth. *Sci. Adv.* **8**, eadd3726 (2022).

62. P. Waidelich, F. Batibeniz, J. Rising, J. S. Kikstra, S. I. Seneviratne, Climate damage projections beyond annual temperature. *Nat. Clim. Change*, 1–8 (2024).

63. T. Amnuaylojaroen, N. Parasin, A. Limsakul, Projections and patterns of heat-related mortality impacts from climate change in Southeast Asia. *Environ. Res. Commun.* **6**, 035019 (2024).

64. W. Chen, X. Lu, D. Yuan, Y. Chen, Z. Li, Y. Huang, T. Fung, H. Sun, J. C. H. Fung, Global PM2.5 Prediction and Associated Mortality to 2100 under Different Climate Change Scenarios. *Environ. Sci. Technol.* **57**, 10039–10052 (2023).

65. A. Ortiz-Bobea, T. R. Ault, C. M. Carrillo, R. G. Chambers, D. B. Lobell, Anthropogenic climate change has slowed global agricultural productivity growth. *Nat. Clim. Change* **11**, 306–312 (2021).

66. K. Tsujimoto, N. Kuriya, T. Ohta, K. Homma, M. S. Im, Quantifying the GCM-related uncertainty for climate change impact assessment of rainfed rice production in Cambodia by a combined hydrologic - rice growth model. *Ecol. Model.* **464**, 109815 (2022).

67. E. K. W. Poon, V. Kitsios, D. Pilcher, R. Bellomo, J. Raman, Projecting Future Climate Impact on National Australian Respiratory-Related Intensive Care Unit Demand. *Heart Lung Circ.* **32**, 95–104 (2023).

68. O. E. Adeyeri, W. Zhou, C. E. Ndehedehe, X. Wang, K. A. Ishola, P. Laux, Minimizing uncertainties in climate projections and water budget reveals the vulnerability of freshwater to climate change. *One Earth* **7**, 72–87 (2024).

69. C. J. Willmott, K. Matsuura, Smart Interpolation of Annually Averaged Air Temperature in the United States. *J. Appl. Meteorol.* **34**, 2577–2586 (1995).

70. K. Schwarzwald, K. Geil, xagg: A Python package to aggregate gridded data onto polygons. *J. Open Source Softw.* **9**, 7239 (2024).

71. Center for International Earth Science Information Network - CIESIN - Columbia University, Gridded Population of the World, Version 4 (GPWv4): Population Density, Revision 11: 2020 (2018).

72. C. Deser, F. Lehner, K. B. Rodgers, T. Ault, T. L. Delworth, P. N. DiNezio, A. Fiore, C. Frankignoul, J. C. Fyfe, D. E. Horton, J. E. Kay, R. Knutti, N. S. Lovenduski, J. Marotzke, K. A. McKinnon, S. Minobe, J. Randerson, J. A. Screen, I. R. Simpson, M. Ting, Insights from Earth system model initial-condition large ensembles and future prospects. *Nat. Clim. Change* **10**, 277–286 (2020).

73. K. Riahi, D. P. van Vuuren, E. Kriegler, J. Edmonds, B. C. O'Neill, S. Fujimori, N. Bauer, K. Calvin, R. Dellink, O. Fricko, W. Lutz, A. Popp, J. C. Cuaresma, S. Kc, M. Leimbach, L. Jiang, T. Kram, S. Rao, J. Emmerling, K. Ebi, T. Hasegawa, P. Havlik, F. Humpenöder, L. A. Da Silva, S. Smith, E. Stehfest, V. Bosetti, J. Eom, D. Gernaat, T. Masui, J. Rogelj, J. Strefler, L. Drouet, V. Krey, G. Luderer, M. Harmsen, K. Takahashi, L. Baumstark, J. C. Doelman, M. Kainuma, Z. Klimont, G. Marangoni, H. Lotze-Campen, M. Obersteiner, A. Tabeau, M. Tavoni, The Shared Socioeconomic Pathways and their energy, land use, and greenhouse gas emissions implications: An overview. *Glob. Environ. Change* **42**, 153–168 (2017).

74. S. I. Seneviratne, M. Hauser, Regional Climate Sensitivity of Climate Extremes in CMIP6 Versus CMIP5 Multimodel Ensembles. *Earths Future* **8**, e2019EF001474 (2020).

75. F. Batibeniz, M. Hauser, S. I. Seneviratne, Countries most exposed to individual and concurrent extremes and near-permanent extreme conditions at different global warming levels. *Earth Syst. Dyn.* **14**, 485–505 (2023).

76. C. P. Morice, J. J. Kennedy, N. A. Rayner, J. P. Winn, E. Hogan, R. E. Killick, R. J. H. Dunn, T. J. Osborn, P. D. Jones, I. R. Simpson, An Updated Assessment of Near-Surface Temperature Change From 1850: The HadCRUT5 Data Set. *J. Geophys. Res. Atmos.* **126**, e2019JD032361 (2021).

77. Z. Hausfather, K. Marvel, G. A. Schmidt, J. W. Nielsen-Gammon, M. Zelinka, Climate simulations: recognize the 'hot model' problem. *Nature* **605**, 26–29 (2022).

78. S. Milinski, N. Maher, D. Olonscheck, How large does a large ensemble need to be? *Earth Syst. Dyn.* **11**, 885–901 (2020).

79. A. J. Cannon, S. R. Sobie, T. Q. Murdock, Bias Correction of GCM Precipitation by Quantile Mapping: How Well Do Methods Preserve Changes in Quantiles and Extremes? *J. Clim.* **28**, 6938–6959 (2015).

80. D. R. Gergel, S. B. Malevich, K. E. McCusker, E. Tenezakis, M. T. Delgado, M. A. Fish, R. E. Kopp, Global Downscaled Projections for Climate Impacts Research (GDPCIR): preserving quantile trends for modeling future climate impacts. *Geosci. Model Dev.* **17**, 191–227 (2024).

81. D. C. Lafferty, R. L. Sriver, Downscaling and bias-correction contribute considerable uncertainty to local climate projections in CMIP6. *Npj Clim. Atmos. Sci.* **6**, 1–13 (2023).

82. P. Kuma, F. A.-M. Bender, A. R. Jönsson, Climate Model Code Genealogy and Its Relation to Climate Feedbacks and Sensitivity. *J. Adv. Model. Earth Syst.* **15**, e2022MS003588 (2023).

83. G. A. Schmidt, D. Bader, L. J. Donner, G. S. Elsaesser, J.-C. Golaz, C. Hannay, A. Molod, R. B. Neale, S. Saha, Practice and philosophy of climate model tuning across six US modeling centers. *Geosci. Model Dev.* **10**, 3207–3223 (2017).

Acknowledgments:

The authors are grateful for insightful conversations with Clara Deser, Amir Jina, Miriam Nielsen, James Rising, Aandishah Samara, and Suzana Camargo. We would like to acknowledge computing support from the Casper system (https://ncar.pub/casper) provided by the NSF

National Center for Atmospheric Research (NCAR), sponsored by the National Science Foundation.

Funding:

National Oceanic and Atmospheric Administration's Regional Integrated Sciences and Assessments Program, grant NA21OAR4310313 (KS, RH)

NSF National Center for Atmospheric Research, via National Science Foundation Cooperative Agreement 1852977 (NL)

Columbia Climate School Postdoctoral Research Program (KS)

Columbia Undergraduate Business Scholars (CUBS) Program (AB)

Columbia Business School's Climate Knowledge Initiative (AB).

Author contributions:

KS conceived of the study. KS designed and performed the analysis, with contributions by AB in running impact models and TB in analyzing how impact modeling decisions interact with observational uncertainty. NL contributed to the design of the study, interpretation of results, and procured computing resources. RH and GW supervised the project, helped with design and interpretation of the results, and acquired funding. KS drafted the manuscript with input and editing from all authors.

Competing interests: Authors declare that they have no competing interests.

Data, code, and materials availability:

All processed data needed to replicate the analysis and figures is available at https://doi.org/10.5281/zenodo.20669397.

The BCD-ME (*18*, *56*, *57*) is freely available via the Earthmover Data Marketplace in Analysis-Ready, Cloud Optimized format (*58*). Additional CMIP6 GCM data was downloaded from the pangeo CMIP6 cloud database. ERA5, GMFD, and JRA-3Q data was accessed via the NCAR filesystem; this data can alternatively be downloaded directly from the publishers instead. MERRA-2 and NLDAS data was downloaded from the NASA GES-DISC interface. UDel data was downloaded from the NOAA PSL gridded data store. PRISM data was downloaded from the PRISM Weather Data store. The Fine-Scaled Weather Dataset was downloaded from Wolfram Schlenker's personal website (*59*). Daymet was downloaded from the NASA Earthdata interface. nClimGrid was downloaded from the National Centers for Environmental Information (NCEI). Berkeley Earth data was downloaded from the Berkeley Earth website.

The replication data for (*29*, *40*, *41*) was taken from each original paper's source.

All code required to replicate the analysis presented in this article is available at https://github.com/ks905383/impact_uncertainty/; a final static version will be published in a frozen format along with this paper.

Additional bias-corrected and downscaled runs were generated using the publicly available replication code for the BCD-ME at https://github.com/ks905383/bcd_me.

Supplementary Materials

Materials and Methods

Supplementary Text

Figs. S1 to S19

Tables S1-S5

References (*60-83*)

Materials and Methods

Fitting dose-response functions

We use three dose-response functions from the climate impacts literature: Carleton et al. (2022) (*29*), relating exposure to daily mean temperature at the ADM2 level to annual all-cause mortality using a quartic polynomial; Burke et al. (2015) (*40*), relating exposure to daily mean temperature at the country level to annual growth in GDP per capita using a quadratic polynomial; and Behrer et al. (2021) (*41*), relating exposure to daily maximum temperature and annual payroll at the U.S. county level using a threshold-defined model. These three dose-response functions have different levels of spatial aggregation, different metrics of temperature, and different functional forms for the dose-response function. Thus, they provide an illustrative sampling of methods used across the empirical climate impacts literature (for details on the relevant factors for assessing observational uncertainty, see fig. S1).

Each of the three applications has a generic formulation for the model used to estimate the causal effect of weather variation:

$$Y = f_r^Y(T_r) + \alpha_r^Y + \varepsilon_r^Y$$

for outcome Y estimated using data from historical gridded weather product r in a functional form $f(\cdot)$ that depends on climate variability $\boldsymbol{T}$ and various fixed effects α and residual ε.

Our aim is to test the sensitivity of these climate impact models to sources of climate uncertainty.

For Carleton et al. (2022) (*29*), we use their simplified age-combined 'pooled' model, which fits one dose-response function for the entire sample (as detailed in their Supplementary Section D.2):

$$f_r^{mortality} = \sum_{k=1}^{4} \beta_{k,r} \sum_{d=1}^{365} T_{r,d}^k + q_r$$

for daily ADM2-level temperature T_d and a country-specific function of daily precipitation q_r, with precipitation represented as a second-order polynomial, summed across the year. We use their preferred age-combined pooled specification, with agegroup-ADM2 and agegroup-country-year fixed effects.

Similar to its use in Carleton et al. (2022) (*29*), the pooled model allows for a more straightforward sensitivity analysis to differing assumptions about climate data. Though the external validity of the model may be limited by the removal of adaptation effects, the pooled model is more stable and reanalysis uncertainty is reduced (see Supplementary Text on the choice of 'pooled' vs. 'interacted' specifications and fig. S12); the magnitude of observational uncertainty would be larger with their preferred model.

For GDP per capita growth, we use the preferred specification of Burke et al. (2015) (*40*) as in their Equation 15:

$$f_r^{\Delta GDP} = \beta_{1,r} T_r + \beta_{2,r} T_r^2 + \beta_{3,r} P_r + \beta_{4,r} P_r^2$$

for population-weighted country average mean annual temperature T and precipitation P.

For payroll, for simplicity, we use the non-dividend, dry-bulb specification of Behrer et al. (2021) (*41*), based on their Equation 2 (specification 1 in their Table SI1):

$$f_r^{payroll} = \beta_{1,r} DA90_r + X_r$$

for days above 90°F *DA90* in each U.S. County, and other climate variables $\boldsymbol{X}$, including annual average precipitation and days in 10°F temperature bins from 0 to 90°F (excluding the 70-80°F bin).

Historical climate data

For each study, we use publicly-available replication code and data, replacing the historical weather data used in $f(\cdot)$ above with new estimates of the same metrics from four reanalysis products: the European Centre for Medium-Range Weather Forecasting's ERA5 (*25*) NASA's MERRA-2 (*26*), the novel Japan Meteorological Agency's JRA-3Q (*27*), and GMFD (*28*, *33*). ERA5, MERRA-2, and JRA-3Q are the three available latest-generation, continuously updating global reanalysis products; we also include GMFD as it is used as the "ground truth" for NASA's NEX GDDP set of bias-corrected and downscaled climate projections. ERA5 (*60–62*), MERRA-2 (*63*, *64*) and GMFD (*29–31*, *65*) have been used extensively to fit climate impact models, as has JRA-3Q's predecessor, JRA-55 (*66–68*). We use daily temperature and precipitation for each product; for MERRA-2, we use the 'bias-corrected precipitation' ('PRECTOTCOR') variable instead of model output precipitation.

As reference, we also use the datasets by Willmott et al. (2001) (*69*) (commonly referred to as "UDel") and PRISM (*48*) to compare results to those by Burke et al. (2015) (*40*) and Behrer et al. (2021) (*41*) in their original papers, respectively.

Our primary results are based on the four reanalyses above, since these are the products used to bias-correct and downscale the BCD-ME, and, especially for the mortality model, which requires global daily temperature, make up a representative sample of the existing products in use for impacts studies. However, other products exist; to test how our results compare to other gridded historical climate records, we show in fig. S11 the GDP per capita growth and payroll models fit with 1 and 4 additional historical data products, respectively. The GDP per capita growth model was additionally fit with temperature data from the Berkeley Earth monthly land temperature record (*44*), referred to as BEST in the figure. Since BEST is a temperature-only record, we use precipitation data from ERA5 in this regression. We additionally fit the payroll model with daily maximum near-surface air temperature data from Daymet (*47*), nClimGrid (*46*), NLDAS (*49*), and Wolfram Schlenker's "Fine-Scaled Weather Dataset" (*59*), which uses the PRISM methodology but with a spatiotemporally homogenous station dataset as input (referred to as "PRISM-Schlenker" in fig. S11). For these regressions, we use precipitation from PRISM.

All products used are listed in Table S4.

Regression parameters and specifications

For our main results, we estimate separate regression coefficients for each reanalysis. To ensure comparability, we fit each model using all years that have data in all reanalyses. This reduces our input sample size, since each historical gridded data product spans a different number of years. GMFD in particular has no mean temperature data available past 2010 and no maximum temperature data past 2008, which especially for the payroll model, can substantially reduce the input sample size. We thus additionally fit each model using all years available for each reanalysis; results are nearly unchanged for mortality and GDP per capita growth and similar for payroll (fig. S3J-L).

We fit each model using reanalysis data re-gridded to a common 0.25-degree grid (the resolution of ERA5 and GMFD) using bilinear interpolation. This is a higher resolution than that of MERRA-2 (0.5 x 0.625-degree) and JRA-3Q (0.375-degree). To test the sensitivity of our results to these differences in resolution, we additionally fit each model using reanalysis data re-gridded to a common 1-degree grid (a lower resolution than the native resolution of all used products), with similar results (fig. S3D-F).

We aggregate gridded reanalysis data to ADM2 (mortality and payroll) or ADM1 (GDP per capita growth) shapefiles using area-weighted averaging, accounting for partial overlaps between grids and polygons using the ***xagg*** package (*70*). We additionally weigh by population density, using 2000 population from the 4th Edition of the Gridded Population of the World (GPW4) dataset, hosted at NASA Earthdata (*71*). We use the 2.5-arc-minute resolution population dataset, and conservatively regrid it to the 0.25-degree grid of the BCD-ME climate data. For mortality and payroll, we calculate nonlinear climate parameters (such as summed polynomial temperature) at the grid cell level before aggregating; for GDP per capita growth we follow the original source and calculate polynomial terms from ADM1-average temperature and precipitation.

To estimate the statistical uncertainty from each regression (as in fig. S3G-I and fig. S4), we fit each model jointly across reanalysis products, interacting each term with a dummy for each reanalysis; this mathematically separates the estimation of regression coefficients across reanalyses (i.e., the coefficients are identical to the case of running a separate regression for each product) but jointly estimates their covariance. Since the different reanalyses are not independent, this avoids overestimating the resulting errors. We sample the resultant regression uncertainty using 1000 draws from a parametric bootstrap from the jointly-normal estimated variance-covariance matrix.

Regression coefficients by input reanalysis or other data products are shown for the main specifications summarized above, using the same calendar years for each product, in Tables S1-3.

Historical product	T (x 10^{-3})	T^2 (x 10^{-3})	T^3 (x 10^{-3})	T^4 (x 10^{-3})
ERA5	-4.54	-1.14***	-38.46	2.85***
	(9.15)	(0.51)	(36.88)	(0.97)
GMFD	-7.73	-1.91***	66.70*	0.01
	(10.95)	(0.63)	(34.09)	(0.79)
JRA-3Q	-7.43	-1.52***	-14.56	2.25***
	(9.07)	(0.49)	(31.30)	(0.83)
MERRA-2	-16.31*	-0.88**	-2.39	1.46**
	(8.73)	(0.44)	(31.96)	(0.73)

Standard errors in parentheses. * p < 0.1, ** p < 0.05, *** p < 0.01.

Table S*1* Regression coefficients for the mortality model. Coefficients shown are for the base regression specifications, using only years (1980-2010) available in all gridded historical products. In the regression, temperature is in degrees C.

Historical product	T (x 10^{-2})	T^2 (x 10^{-4})	P (x 10^{-5})	P^2 (x 10^{-9})
ERA5	1.54***	-5.69***	1.28	-4.31**
	(0.47)	(1.30)	(1.03)	(1.95)
GMFD	1.92***	-5.91***	10.96*	-38.61
	(0.61)	(1.58)	(6.44)	(35.34)
JRA-3Q	1.48***	-5.98***	1.15	-5.08**
	(0.48)	(1.41)	(1.12)	(2.39)
MERRA-2	1.31**	-4.17***	-0.00	-0.60
	(0.55)	(1.40)	(0.72)	(0.63)
UDel	1.37***	-4.93***	1.62	-5.33*
	(0.46)	(1.29)	(1.19)	(3.02)

Standard errors in parentheses. * p < 0.1, ** p < 0.05, *** p < 0.01.

Table S*2* Regression coefficients for the GDP per capita growth model. Coefficients shown are for the base regression specifications, using only years available in all gridded historical products (1980-2010). In the regression, temperature is in degrees C and precipitation is in mm/day.

5

Historical product	# days > 90F (x 10^{-4})	P (x 10^{-3})
Daymet	-5.78***	-2.74*
	(1.24)	(1.47)
ERA5	-1.87	2.11
	(1.15)	(1.62)
GMFD	-1.52	-1.41
	(1.22)	(1.37)
JRA-3Q	-4.44***	-4.11**
	(1.18)	(1.80)
MERRA-2	-4.36***	-1.93
	(1.08)	(1.56)
NLDAS	-6.72***	-6.25***
	(1.15)	(1.48)
PRISM	-4.11***	-3.07**
	(1.18)	(1.46)
PRISM-Schlenker	-5.38***	-2.63*
	(1.21)	(1.48)
nClimGrid	-2.99**	-1.54
	(1.22)	(1.50)

Standard errors in parentheses. * p < 0.1, ** p < 0.05, *** p < 0.01.

Table S*3* Regression coefficients for the payroll model. Coefficients shown are for the base regression specifications, using only years available in all gridded historical products (1986-2008). In the regression, precipitation is in units of mm/day.

Sensitivity of impact models to precipitation data

All three impact models analyzed here use annual precipitation as a control. To estimate the sensitivity of these models to precipitation inputs, we create cross-estimates of dose-response functions across reanalyses using temperature and precipitation from all four reanalyses and additionally UDel and PRISM for GDP per capita growth and payroll, respectively (fig. S12). For example, we fit the mortality dose-response function using ERA5 temperature, but ERA5, MERRA-2, JRA-3Q, and GMFD precipitation. The mortality model is largely insensitive to the choice of rainfall data. The GDP per capita growth model is only substantially changed by the use of UDel precipitation. The payroll model is more sensitive to the choice of precipitation data, but shuffling precipitation inputs generally does not change the ordering of products by projected damages.

Note, however, that for especially the mortality and GDP per capita growth models, coefficients on precipitation controls may vary widely between products without substantially changing the overall dose-response function (Tables S1-S3).

Projections of climate impacts

We generate projections of climate impacts by inputting changes in mean (mortality and GDP per capita growth) or maximum (payroll) daily temperature between historical and future periods from GCMs into the impact models described above. Since GCMs are coarse in resolution and "biased" in their mean states and higher moments compared to the real world, we require bias-corrected and downscaled GCM output. For consistency with the dose-response functions (since, given differing native resolutions and model characteristics, impacts of exposure to a given climate state trained on a particular reanalysis are not exactly comparable or interchangeable with those trained on other historical gridded data products), these projections must be bias-corrected and downscaled to the same reanalyses used in training the impact models.

To fully estimate the climate uncertainty in these projections, we additionally require climate projections that adequately sample model uncertainty and internal variability, in addition to accounting for scenario uncertainty.

Future BCD-ME climate projections

We primarily use the novel Bias-Corrected and Downscaled Massive Ensemble (BCD-ME (*18*)) a set of over 1,400 projections of daily mean and maximum temperature developed for the express purpose of diagnosing uncertainty in projections of climate impacts. This ensemble is based on "Large Ensembles" of GCMs (see Table) from the 6th Phase of the Coupled Model Intercomparison Project (CMIP6; the current state-of-the-art set of GCMs), which sample internal variability by providing multiple model runs for each greenhouse gas forcing scenario, with initial conditions slightly varied between ensemble members (*72*). Due to the chaotic nature of the climate system, these runs quickly diverge to span a broad range of possible climate states for a given set of forcings.

To focus on aspects of uncertainty in climate data alone, the BCD-MEs correct for scenario uncertainty by using climate data in 20-year increments organized by Global Warming Level (GWL) rather than by calendar year. In other words, data from any Shared Socioeconomic Pathway (SSP, (*73*)) is taken, and its calendar year axis is translated into global mean surface

temperature anomalies vs. its 1850-1900 average. Following Seneviratne and Hauser (2020) (*74*) and Batibeniz et al. (2023) (*75*), for each climate model ensemble member we calculate the global mean surface annual temperature anomaly and compute a 20 year moving average. Then, for each GWL, we find the first year that this moving average crosses the given GWL, and define the 20 years around this year as the climate for this GWL. We thus produce 20-year time series for GWLs 0.61 (following Seneviratne and Hauser (2020) (*74*), representing 1982-2001 in the real world—as estimated by the HadCRUT5 (*76*) dataset—as a reference time period) and in 0.5-degree increments for as many GWLs as are crossed in a given simulation. For reference, in HadCRUT5, GWL1 reflects 2001-2020 in the real world. Since the BCD-ME outputs 20-year average statistics of the climate, all impacts projections are calculated as the impact due to the average annual climate across these 20 years.

By normalizing across GWLs, the BCD-ME has allowed us to consciously ignore scenario uncertainty and focus on uncertainty in the climate data itself. Our choice also avoids the difficulties in accurately estimating scenario uncertainty, which, besides depending nontrivially on the subjective choice of scenarios is also hampered by the limited number of GCMs that have published data from multiple runs over all desired scenarios.

The use of GWLs implies that metrics of interest vary only with average warming and are not pathway-dependent (and thus scenario-dependent at a given level of warming). This is the case for temperature and across the ScenarioMIP experiments (*18*, *74*). Thus, GWLs, in addition to controlling for scenario uncertainty, provide a way to study future impacts that is agnostic to climate sensitivity, helping avoid the so called "hot model"' problem from GCMs with unphysically high climate sensitivities in CMIP6 (*77*). Furthermore, we are thus able to boost the ensemble size for each GCM by pooling runs based on different SSPs, allowing for better accounting of internal variability, since otherwise many large ensembles have data available for fewer ensemble members per SSP than are necessary to characterize internal variability (see, e.g., (*78*)). Removing climate sensitivity does, however, reduce the influence of model uncertainty compared to projections indexed by year; we test the magnitude of this effect in the Methods section on additional climate projections by year and fig. S9.

The BCD-ME uses Quantile Delta Mapping (QDM (*79*)) to bias-correct GCM runs to each reanalysis, using maps by day-of-year (with a 31-day moving average) between empirical quantiles of GCMs and reanalyses to account for fine-grained, non-parametric shifts in climate distributions. The baseline for this mapping is conducted at GWL0.61 in both models and reference reanalysis datasets; we thus assume that, at the same GWL, the real climate and the climate of a GCM run are equivalent draws from an underlying distribution of internal variability, with the evolution of the ensemble member between GWL0.61 and warmer climates representing not only global warming, but also that ensemble member's evolution of patterns of internal variability.

The BCD-ME uses Quantile-Preserving Localized Analog Downscaling (QPLAD (*80*)) to downscale 1-degree bias-corrected runs to the 0.25-degree resolution needed. For each reanalysis, a downscaling map from 1 to 0.25 degrees is calculated as the difference between the empirical cumulative distribution functions (CDFs) at the two scales, and then applied to each GCM run, downscaling each value based on the downscaling map for its quantile and day-of-year. As before, CDFs are calculated by day-of-year using a 31-day rolling average across years centered on that day-of-year.

We show that the downscaling procedure does not affect our primary results by also replicating them using 1-degree-resolution bias-corrected data in fig. S8.

Uncertainties from bias-correction and downscaling methodologies

Our projections of climate impacts are based on the BCD-ME, which uses one of a wide range of commonly-used methodologies to bias-correct and downscale future climate projections. Lafferty and Sriver (2023) (*81*) show that this choice of post-processing method can have a substantial impact on total uncertainty and thus the total climate uncertainty in our projections is still likely underestimated. However, since our primary conclusions hold even when only considering the spread across dose-response functions trained on different reanalyses (Fig. 4), we expect the choice of historical gridded data product to outweigh model uncertainty and internal variability for much of the globe regardless of the method used to post-process GCM output.

Regions for projected impacts

We aggregate projected nonlinear climate metrics from the 0.25-degree BCD-ME grid to the regional level. For projections of mortality, we use the custom "impact regions" of Carleton et al. (2022) (*29*) which consist of 24,378 sets of political regions that are roughly internally consistent in terms of climate and roughly comparable in terms of population. For projections of GDP per capita growth (global ADM0) and payroll (ADM2 in the continental United States), we use the same regions that were used to fit the corresponding models.

For simplicity and to isolate uncertainty in climate data, we assume populations and population structure remains constant from the historical training period. As before, aggregate the gridded climate data to these regions using the ***xagg*** (*70*) package. We additionally weigh by the same constant 2000 population densities used to aggregate reanalysis data; since we are interested primarily in the sources of climate uncertainty in these projections, keeping the population geography constant avoids introducing additional scenario uncertainties.

Samples of GCMs and ensemble members

We first verify that we adequately sample internal variability. We calculate the minimum number of runs needed to characterize the internal spread of a GCM by, for each GCM, resampling impact projections across ensemble members with replacement for an increasing sample size. For each sample size n (with n reaching from 2 ensemble members to the maximum number of ensemble members N available), we draw 100 subsets of n ensemble members and calculate the variance across each subset. As n increases, the mean across subset variances eventually converges to a value we term the "final" or "true" internal variability, and which we estimate as the mean across the mean variance over the last 5 sample sizes, i.e., from $n = N\text{-}5$ to $n = N$.

Fig. S5 shows maps of the maximum across GCMs of the n needed to reach 85% of the "final" internal variability, in other words, a metric of how many ensemble members per GCM are needed to adequately characterize internal variability. The largest "Large Ensemble" (CanESM5) in the BCD-ME contains 86 ensemble members, giving a wide range of n for which to test the stability of estimates of internal variability. We show in fig. S4 that, for each impact, the required n is 13 or less for the vast majority of regions.

We then verify that we adequately sample model uncertainty. Unlike for internal variability, for which each GCM ensemble member is a quasi-random sample, each GCM is not a random sample across the model uncertainty of a generation of GCMs. GCMs share code and have common ancestors along a limited set of 'genealogies' (*82*), some GCMs are 'tuned' to common metrics such as top-of-atmosphere energy balances (*83*) and some models have systemically different climate sensitivities than others (*77*). The BCD-ME provides data for the 12 CMIP6 models that have been run with many ensemble members as Large Ensembles, but we must not only identify how many GCMs are needed to sample the spread across the BCD-ME, but whether the BCD-ME adequately samples the spread across GCMs of the latest generation.

To do so, we expand the BCD-ME using one run each of an additional 10 GCMs (see Table) representing in total all GCMs with daily mean and maximum temperature available on the Pangeo cloud data store (https://gallery.pangeo.io/repos/pangeo-gallery/cmip6/) and a larger subset of the full CMIP6 spread. These projections are processed in the same way the original BCD-ME ensemble members are. Similar to before, we draw 100 sets of m GCMs with replacement, with m increasing from 2 to $M=22$, the total number of GCMs tested, and calculate model uncertainty for each subset as the variance across GCMs. Since in our sample only the GCMs in the BCD-ME have data for many ensemble members, we randomly draw a run from each GCMs chosen in a particular subset. Though the variance across a subset therefore captures both model uncertainty across GCMs and internal variability implicit across random draws from each GCM, this comparison is preferable to taking the mean across ensemble members for Large Ensembles, which would result in artificially reduced variability for the BCD-ME sample vs. the 22-GCM sample.

As before, as m increases, we expect the variance across subset variances to eventually converge to a "final" model uncertainty, which we estimate as the mean across the mean variance over the last 5 sample sizes, i.e., from $m = 22\text{-}5$ to $m = 22$. Since this method by necessity samples both model uncertainty and internal variability, convergence is slower than across runs within a GCM, with a large range of estimated model uncertainties within each subset (fig. S6 right panels, shaded areas). Nevertheless, for the vast majority of regions, on average fewer than 8 GCMs are needed to reach 85% of the `final' uncertainty (fig. S6, maps), and the uncertainty across the BCD-ME sample is representative of the uncertainty across the full 22 GCMs tested (fig. S6, hatching in maps and right panels).

We therefore feel confident that, on average, we are adequately sampling both model uncertainty and internal variability.

Since GCMs have different climate sensitivities, not all BCD-ME runs reach all GWLs. Additionally, each GCM in the BCD-ME has a different number of ensemble members. To allow for self-consistent comparisons across models and GWLs, unless otherwise labeled, figures are based on 13 randomly chosen ensemble members from the 8 GCMs that have at least 13 ensemble members reach GWL2.5 (10 ensemble members from 7 GCMs for payroll, since the BCD-ME has fewer data for maximum temperature), with figs. S7-9 and S16-19 showing results based on all available runs from all BCD-ME GCMs; results are similar between these and main text figures, as would be expected if uncertainties are adequately sampled.

Additional climate projections by year

The BCD-ME is organized by GWL, abstracting away from scenario uncertainty and allowing ensemble members from any SSP to be used to boost the sample size across which to estimate

internal variability. However, in doing so, a substantial driver of intermodel differences, namely differences in climate sensitivities, is removed from estimates of model uncertainty. Main text Fig. 3 therefore is based on estimates of model uncertainty that are lower at a given GWL than they would be at a given year.

However, projections of climate impacts are often required as estimates for a particular set of years or lead times. To test the relative importance of different sources of climate uncertainty in this context, we create up to 91 new bias-corrected 1-degree-resolution climate projections for several 20-year periods from up to 11 GCMs, using every available ensemble member run using SSP2-4.5 available on the pangeo online data store. We replicate the BCD-ME methodology, but train bias-correction maps on the 1982-2001 period in both reanalyses and GCMs, and project mean and maximum daily temperature using the 20-year periods 2000-2019, 2030-2049, and 2060-2079 vs. 1982-2001 instead of GWLs vs. GWL0.61. Results are shown in fig. S9 and S19.

Projecting impacts for UDel and PRISM

In the right column of Fig. 2, we show distributions across the ensemble of global or CONUS-average impact projections, split up by the original historical gridded product used in each paper and the full BCD-ME ensemble. Since the BCD-ME does not contain projections bias-corrected and downscaled to UDel and PRISM (the original products used in Burke et al. (2015) (*40*) and Behrer et al. (2021) (*41*), respectively), we create these projections by using the dose-response function fit using UDel or PRISM and the future climate states from each of the BCD-ME reanalyses, showing the mean across these products. Since most of the reanalysis uncertainty comes from the original fitting of the dose-response function rather than the bias-correction and downscaling procedure (Fig. 4), these projections (in blue in Fig. 2F, I) are largely robust to the choice of bias-correction and downscaling target.

Partitioning uncertainty

We estimate the relative contribution of sources of uncertainty to the spread in projections of climate impacts using the Law of Total Variance (*42*). Model uncertainty is estimated as the variance across model mean projections and internal uncertainty as the mean variance of projections across ensemble members within models.

We sample 'observational' uncertainty over four reanalysis products. We refer to this in the text as 'reanalysis' uncertainty to emphasize its origin as coming from one specific class of products commonly used as estimates of historical weather patterns. For the purposes of this study, we assume flat priors over the reanalyses and measure observational uncertainty as the mean variance across realizations associated with each reanalysis (i.e., that used a particular reanalysis for fitting the statistical model and bias-correcting and downscaling the climate projections).

In fig. S4, we additionally estimate the contribution of regression uncertainty, which we calculate as the mean across ensemble members and reanalysis products of the variance across 1000 Monte Carlo draws of coefficients from their covariance matrix.

Since in particular model and internal variability are not fully independent and orthogonal (different GCMs have different internal variability distributions), the sum of these estimates will not exactly sum to the variance across the total ensemble. However, the resultant cross-terms are generally assumed to be small and are commonly ignored (*42*). In any case, this partitioning in

sources of uncertainty allows a diagnosis of where geographically and for which lead times a given source of uncertainty substantially contributes to the spread in future climate risk.

Partitioning reanalysis uncertainty

Uncertainty due to the choice of gridded historical data product can enter projections of climate impacts both through the fitting of the statistical impact function and through the GCM post-processing (bias-correcting and downscaling) procedure. To isolate which of these pathways dominates, we create cross-estimates of future impacts across reanalyses using all four dose-response functions and all four sets of bias-corrected and downscaled simulations (Fig. 4). In other words, we take the dose-response function fit using the reanalysis products ERA5, MERRA-2, JRA-3Q, and GMFD and use each to project damages using GCM output bias-corrected and downscaled to all of ERA5, MERRA-2, JRA-3Q, and GMFD, creating 16 sets of future damage estimates.

We then calculate the average variance across bias-corrected and downscaled runs, holding dose-response estimation fixed, and vice-versa, calculating the variance across dose-response estimations while holding bias-correction and downscaling ground truth fixed. Comparing the ratio between these two variances for a location identifies whether the spread in future damages is affected more by differences in dose-response functions or by differences in bias-correction and downscaling algorithms.

Choice of 'pooled' vs. 'interacted' specification for Carleton et al. (2022)

For Carleton et al. (2022) (*29*), using public replication data leads to discrepancies with the original paper, since part of their replication data (mortality data from the USA and China) were not shared publicly due to restrictive access agreements with the data providers. The publicly available sample size is strongly reduced relative to the sample used in the original analysis, leading to unstable model behavior in some parts of the world for their `preferred' specification, which contains interactions with income and long-run temperature (and whose results are shown in e.g., their Figure IV). Because of this instability, the model is highly sensitive to the choice of input data and the dominant source of uncertainty is trivially due to the spread across reanalyses (fig. S15).

The impact of individual reanalyses on estimates of observational uncertainty

To determine the impact of individual reanalyses on estimates of observational uncertainty, we conduct a leave-one-out analysis in calculating reanalysis uncertainty. We re-estimate reanalysis uncertainty for each impact, calculated across impact projections based on three out of the four reanalyses studied at a time. For each reanalysis, we then take the difference between the reanalysis uncertainty calculated without it and the reanalysis uncertainty calculated across all four reanalyses, and extract the reanalysis for which this difference is largest. This product is shown for every location and impact in fig. S16. All four reanalyses studied have locations and impacts for which they are the largest driver of reanalysis uncertainty.

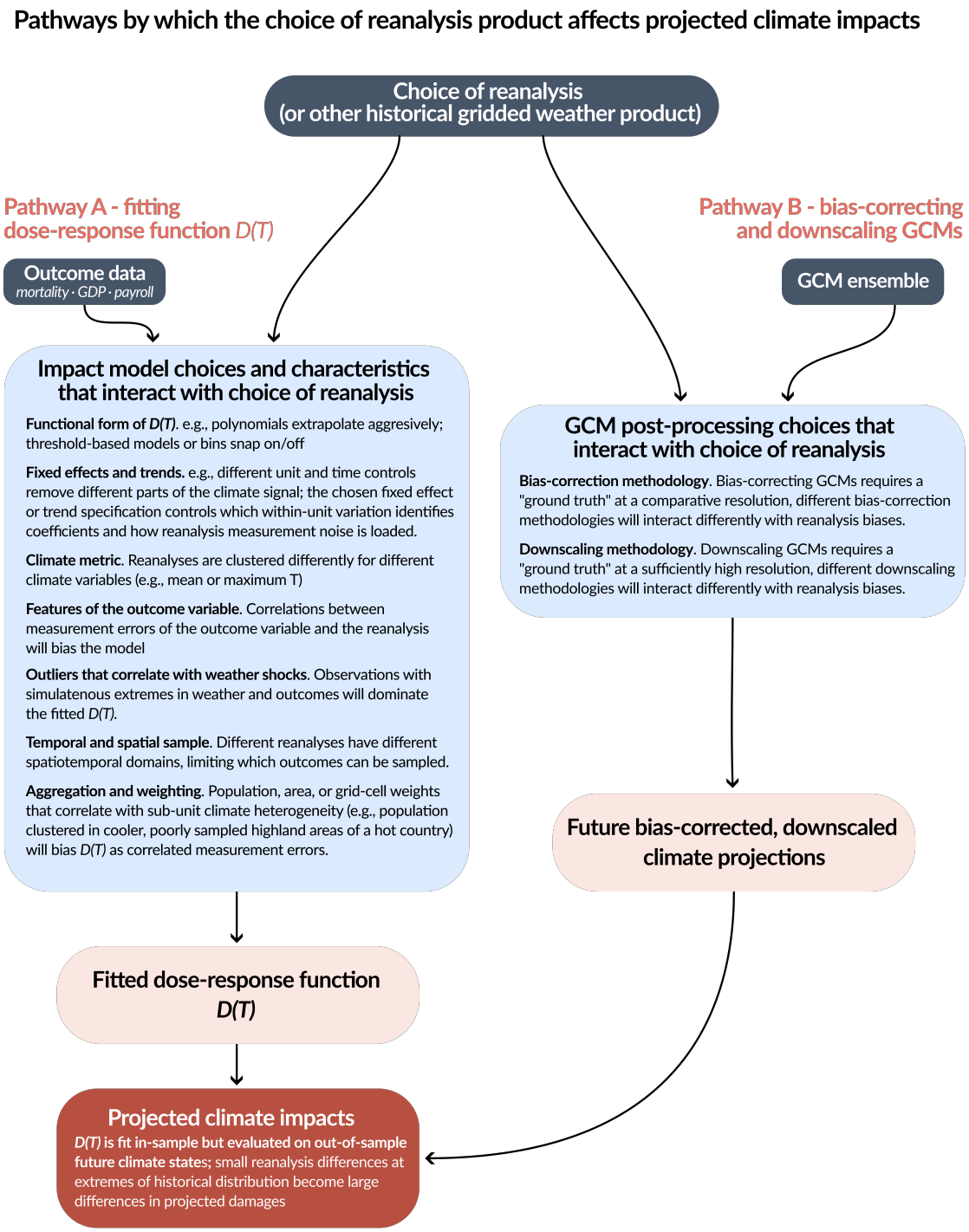


Fig. S1. Pathways by which the choice of reanalysis product affects projected climate impacts. Diagram of how the choice of reanalysis product interacts with fitting dose-response functions (left side) and post-processing GCM output (right side) to produce reanalysis uncertainty in future projections of climate impacts.

5

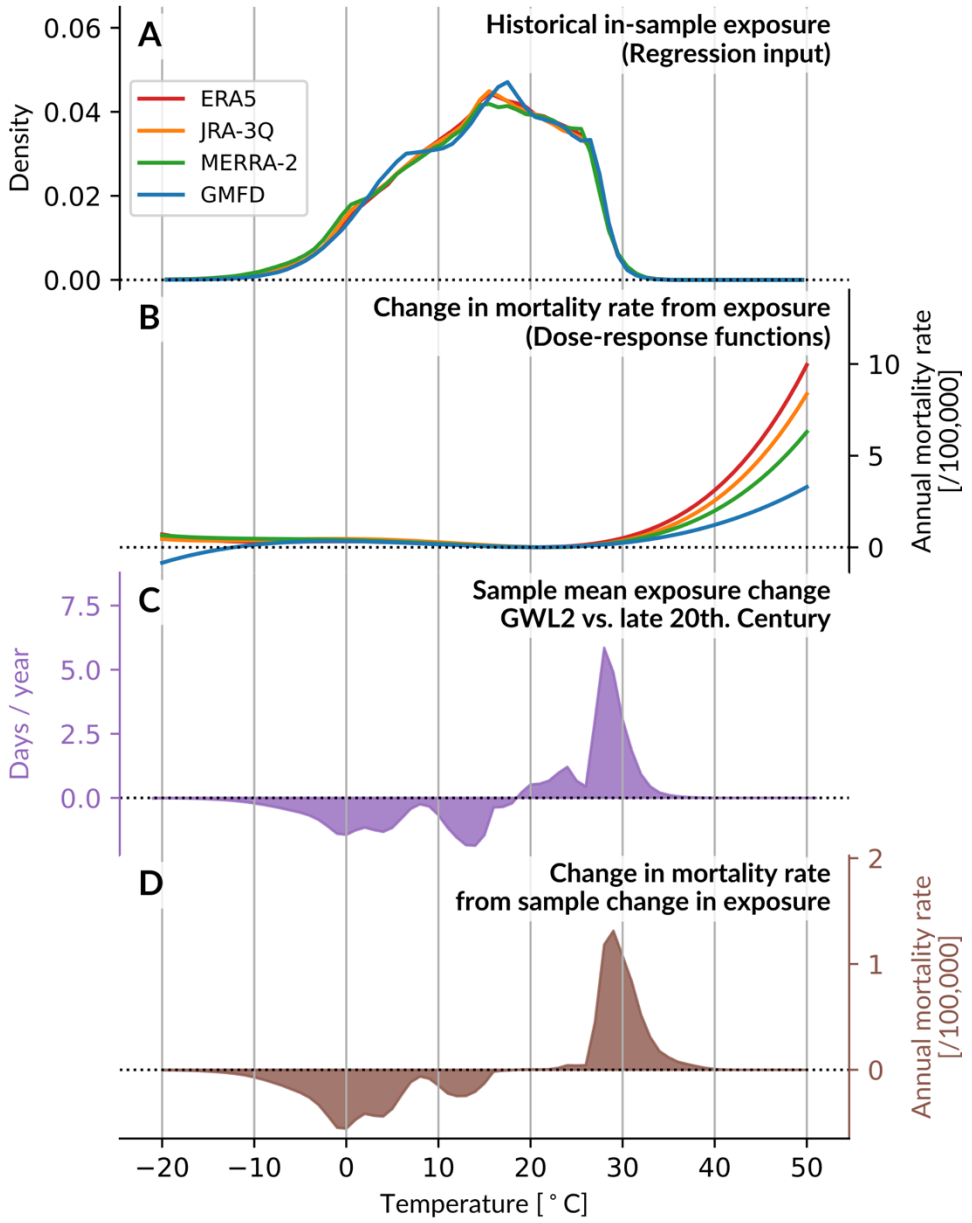


Fig S2. Version of main text Fig. 1 showing in-sample exposure and mortality rate changes. As in Fig. 1, but with changes in temperature exposure **(C)** and contribution to changes in mortality rate by temperature (**D**) averaged only over regions used in fitting the temperature-mortality relationship in **B** (i.e., the regions highlighted in yellow in Fig. 2B). As in Fig. 1, the population-weighted historical temperature distribution over these regions is shown for each reanalysis product in **A**.

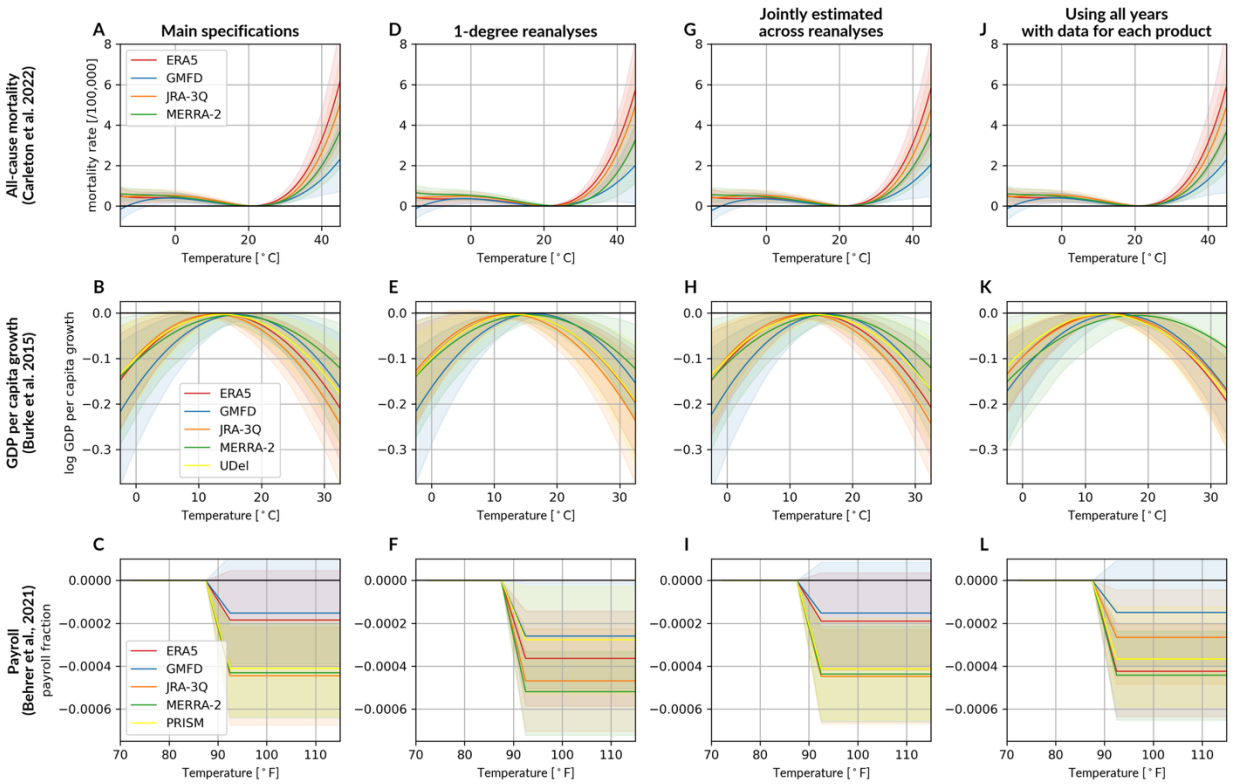


Fig. S3. Dose-response functions fit using alternate specifications. Dose-response functions as in Fig. 2A, D, G, fit using alternate specifications: using 1-degree instead of 0.25-degree input data (**D-F**) with errors jointly estimated across reanalyses in an interacted model instead of separate regressions (**G-I**), using all years for each reanalysis instead of only years available in all reanalyses (**J-L**). Panels (A-C) are identical to the left column of main text Fig. 2, for reference. See fig. S8 for uncertainty partitioning of damage projections using the 1-degree dose-response functions of panels (D-F).

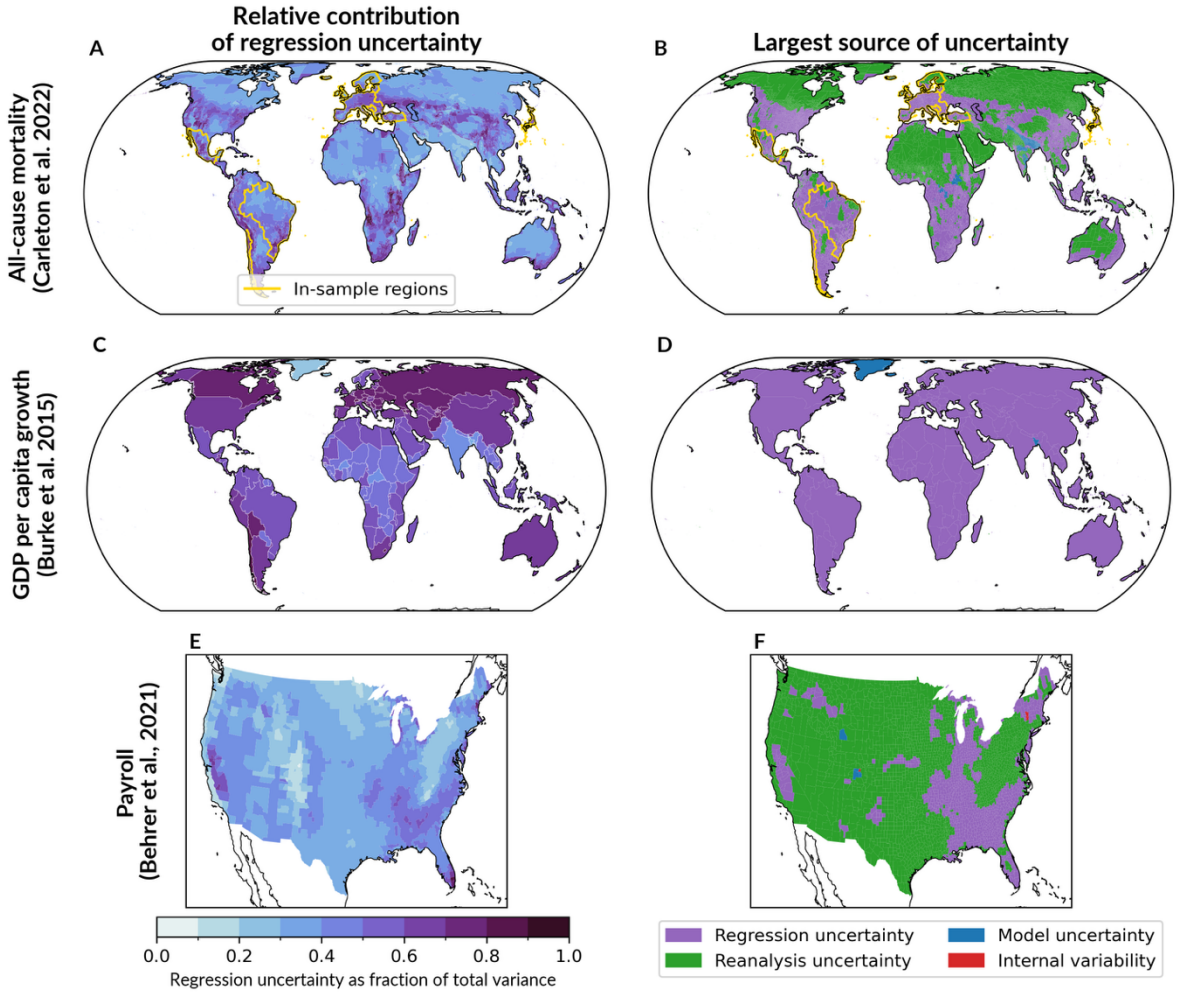


Fig. S4. Regression vs. climate uncertainty. Fraction of total variance contributed to by regression uncertainty (left column) and dominant source of uncertainty with regression uncertainty included (right column) for three analyzed impact models, for projected changes between GWL0.61 and GWL2. Regression uncertainty contributes a total population-weighted average 45%, 65%, and 34% to the spread in projections of mortality, GDP per capita growth, and payroll, respectively (42%, 60%, and 37% when weighted by area). The yellow lines in panels (**A**) and (**B**) show which countries were included in the regression.

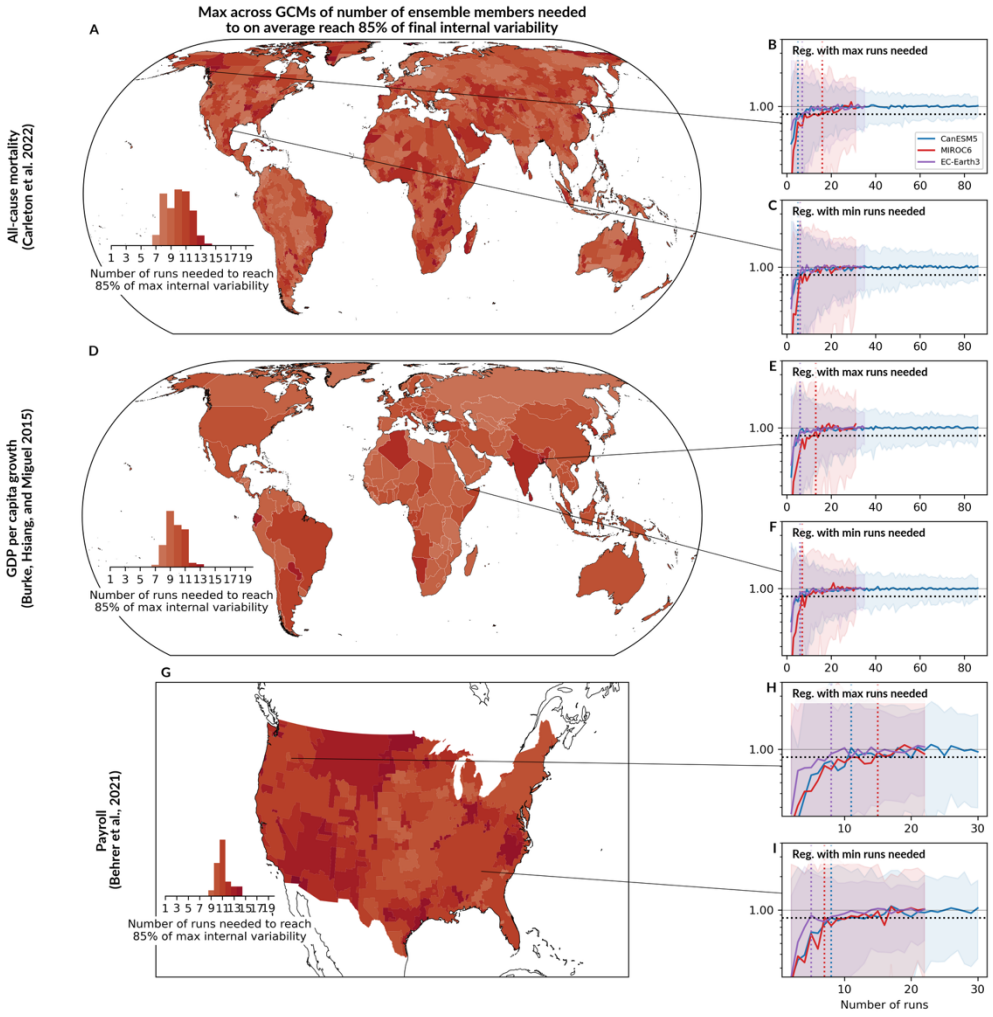


Fig. S5. Sampling of internal variability. The maximum number of ensemble members needed to reach 85% of the maximum internal variability (maps) and evolution of estimates of internal variability by sample size for sample locations for the 3 GCMs with the most runs in the BCD-ME (CanESM5, MIROC6, and EC-Earth3), normalized by the mean internal variability calculated over the last 5 sample sizes (right panels) for each impact model for changes between GWL0.61 and GWL2. For reach region, the number of ensemble members needed to characterize internal variability is calculated for each GCM separately, and the maximum is taken across GCMs. The shading in the illustrative panels shows the range of internal variability estimated as the mean variance across 100 Monte Carlo draws with replacement of x ensemble members of a GCM, with the sample size x given by the x-axis. The y-axes in the illustrative panels are logarithmic, such that 2x the `final' internal variability is equally distant from 1 as 1/2x that value. See the Methods section on samples of GCMs and ensemble members for details.

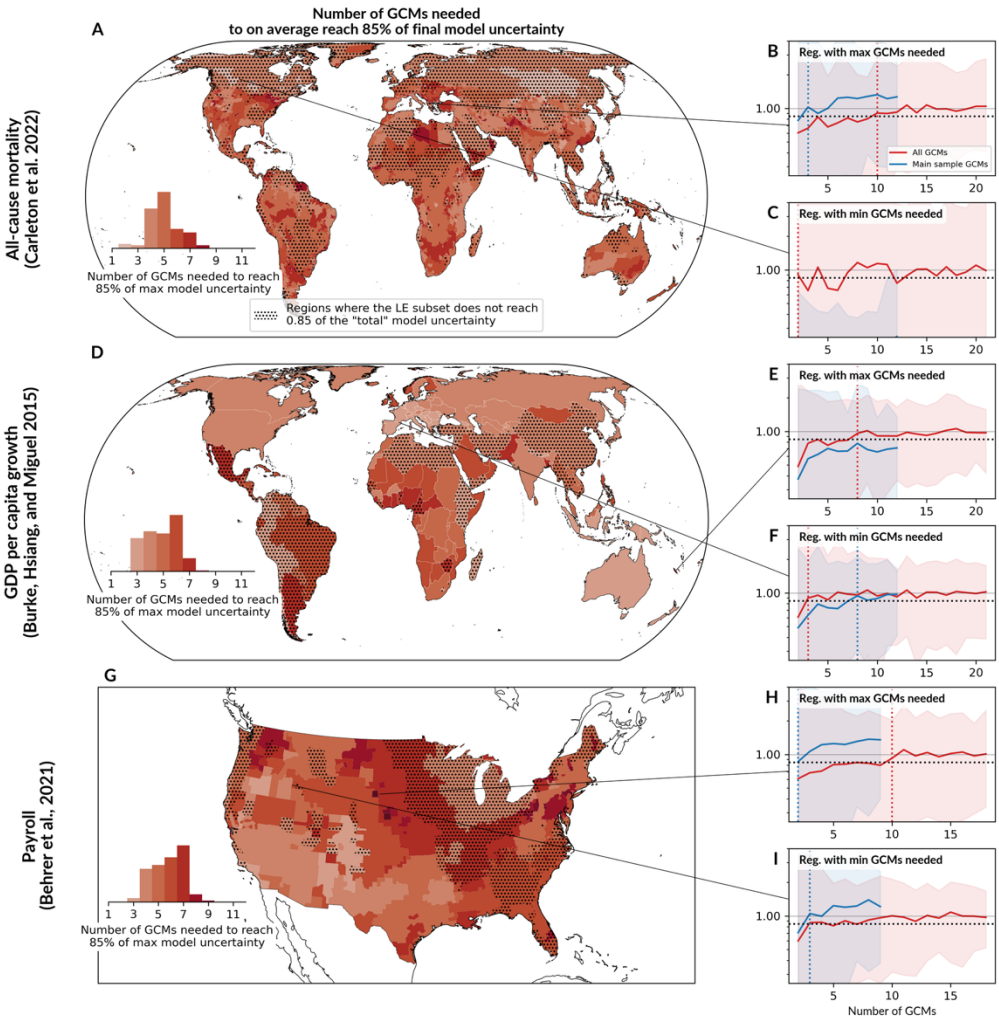


Fig. S6. Sampling of model uncertainty. The number of GCMs needed to reach 85% of the maximum model uncertainty (maps) and evolution of estimates of model uncertainty by sample size for sample locations for the main-text sample GCMs from the BCD-ME (blue) and the larger 24-GCM sample (red), normalized by the mean model uncertainty calculated over the last 5 sample sizes (right panels) for each impact model for changes between GWL0.61 and GWL2. The hatching shows where the main-text sample of GCMs does not reach at least 85% of the "total" model uncertainty estimated across 24 CMIP6 GCMs, though we note that the model uncertainty across the main text sample also exceeds that of the 24-GCM sample in many locations. The shading in the illustrative panels shows the range of model uncertainty estimated as the mean variance across 100 Monte Carlo draws with replacement of one ensemble member each of *x* GCMs, with the sample size *x* given by the x-axis. The y-axes in the illustrative panels are logarithmic, such that 2x the `final' internal variability is equally distant from 1 as 1/2x that value. See the Methods section on samples of GCMs and ensemble members for details.

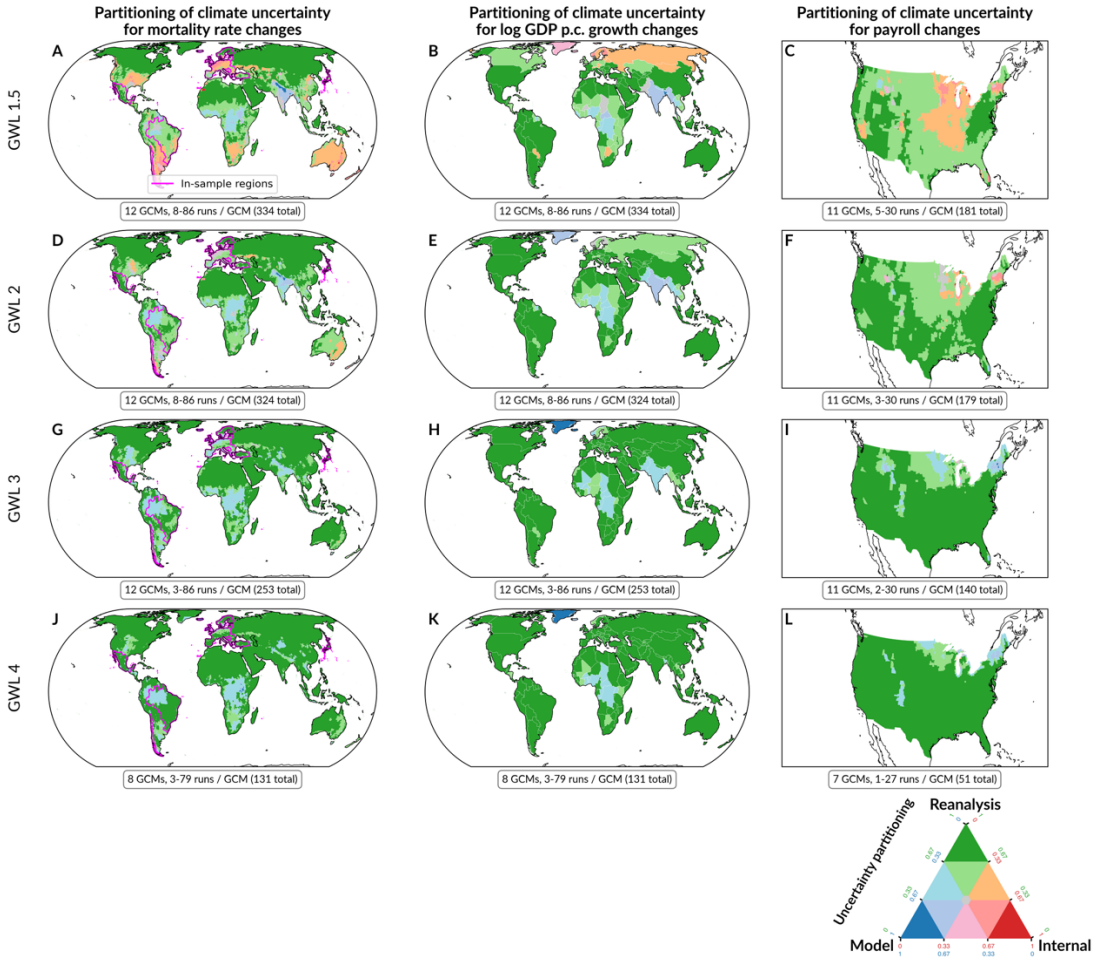


Fig. S7. Uncertainty partitioning across GWLs using all BCD-ME runs. Uncertainty partitioning as in Fig. 3, but using all available runs and GCMs for each GWL instead of a consistent panel of ensemble members. See fig. S17 for a version showing the largest individual source of uncertainty instead, in a colorblind-friendly figure.

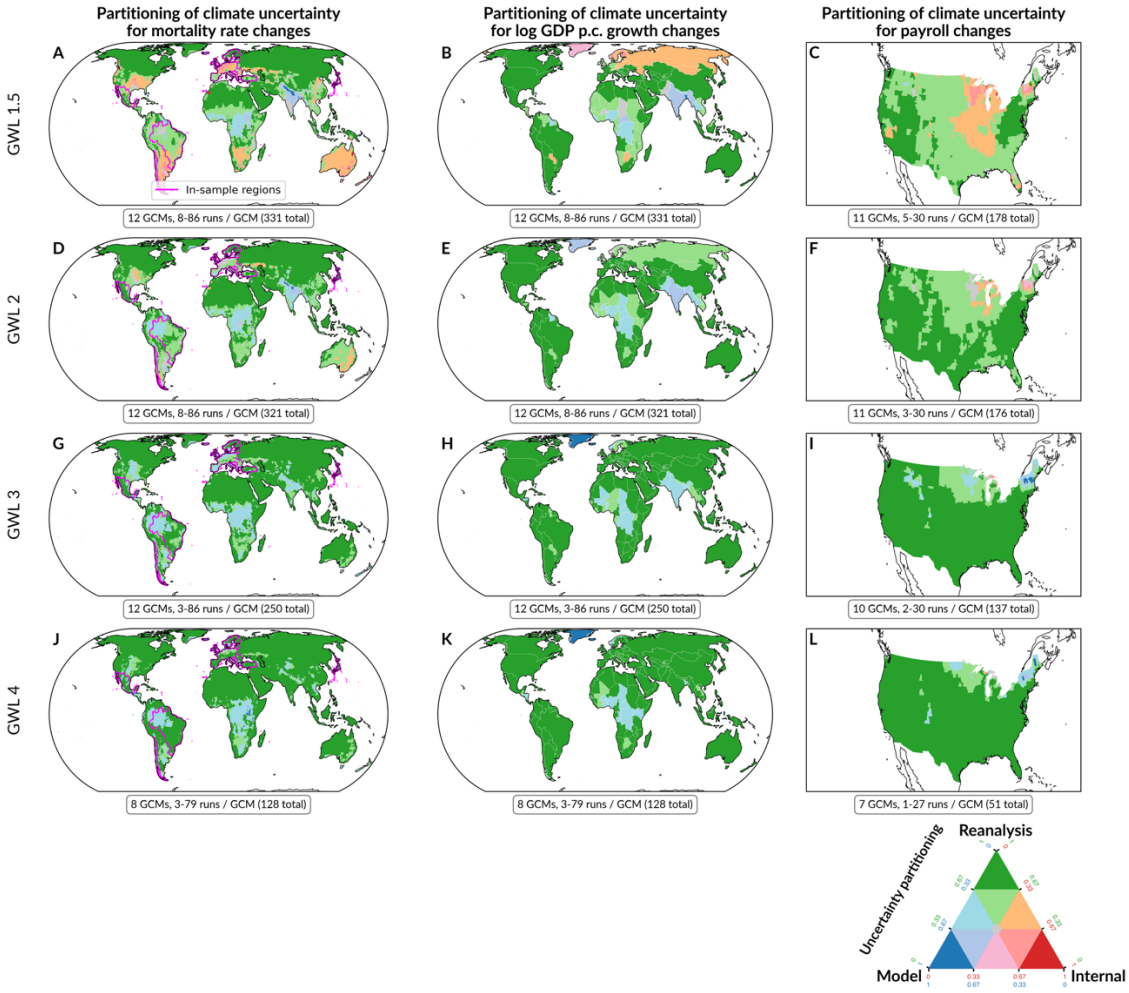


Fig. S8. Uncertainty partitioning using 1-degree historical and future climate data. Uncertainty partitioning as in Fig. 3 and fig. S7, but using climate projections and reanalyses aggregated to a 1-degree instead of an 0.25-degree latitude/longitude grid. See fig. S18 for a version showing the largest individual source of uncertainty instead, in a colorblind-friendly figure.

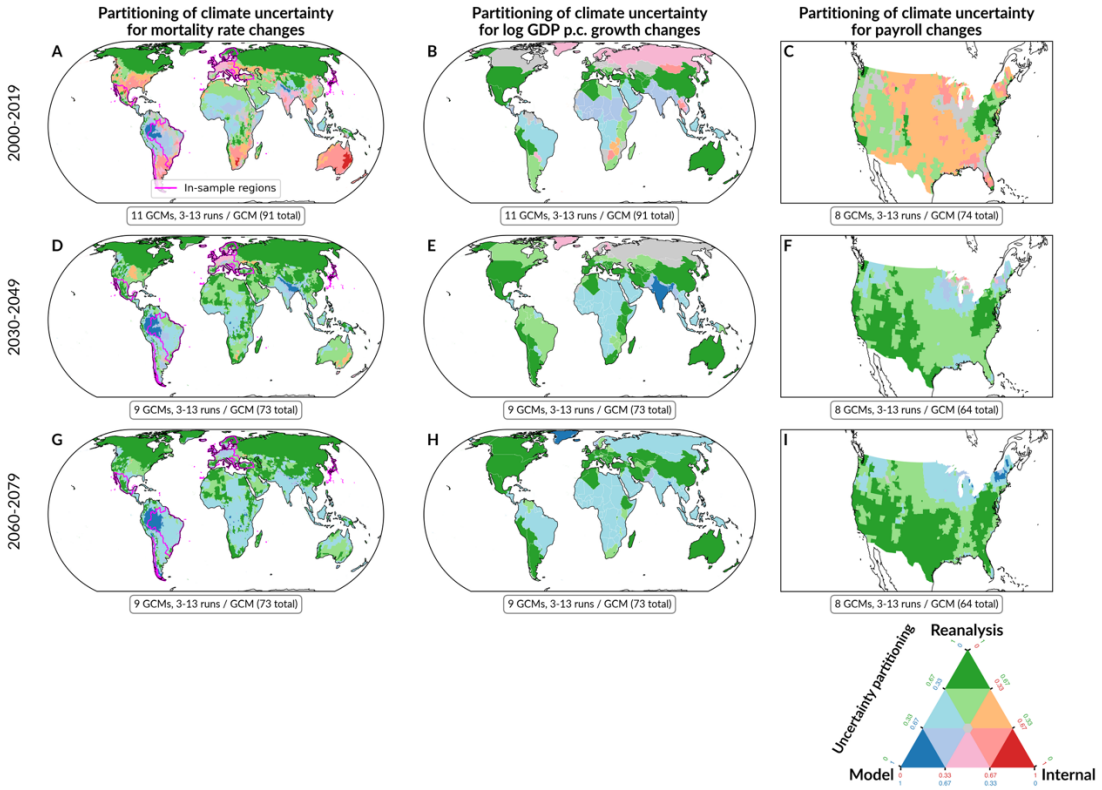


Fig. S9. Uncertainty partitioning by year instead of by GWL. Uncertainty partitioning as in Fig. 3 and fig. S8, but using climate projections between 1982-2001 and 2000-2019, 2030-2049, and 2060-2079 instead of by GWL. Note the smaller sample size compared to GWL-based projections. All ensemble members used in this calculation use the SSP2-4.5 scenario. For projections to 2030-2049, observational uncertainty is the largest source of climate uncertainty for 86%, 67%, and 93% of locations by area for mortality, GDP per capita growth, and payroll, respectively (compare to 93%, 89%, and 98% for projections to GWL2), or 68%, 71%, and 90% of locations by population (compare to 78%, 78%, 96% for projections to GWL2). See the Methods section on additional climate projections by year for details. See fig. S19 for a version showing the largest individual source of uncertainty instead, in a colorblind-friendly figure.

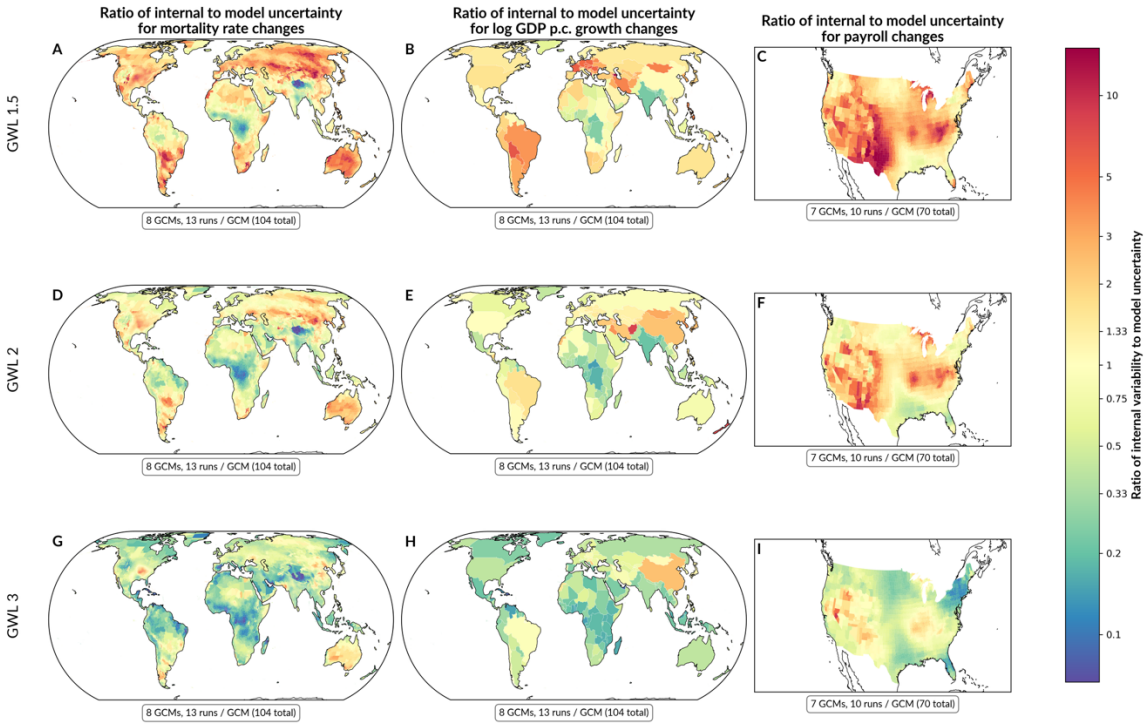


Fig. S10. Relative importance of internal variability vs. model uncertainty in impacts projections. Ratio of internal variability to model uncertainty in projections of climate impacts between GWL0.61 and GWLs 1.5-3, using the same consistent sample of ensemble members as in Fig. 3. Internal variability is larger than model uncertainty for reddish regions and vice-versa for bluish regions.

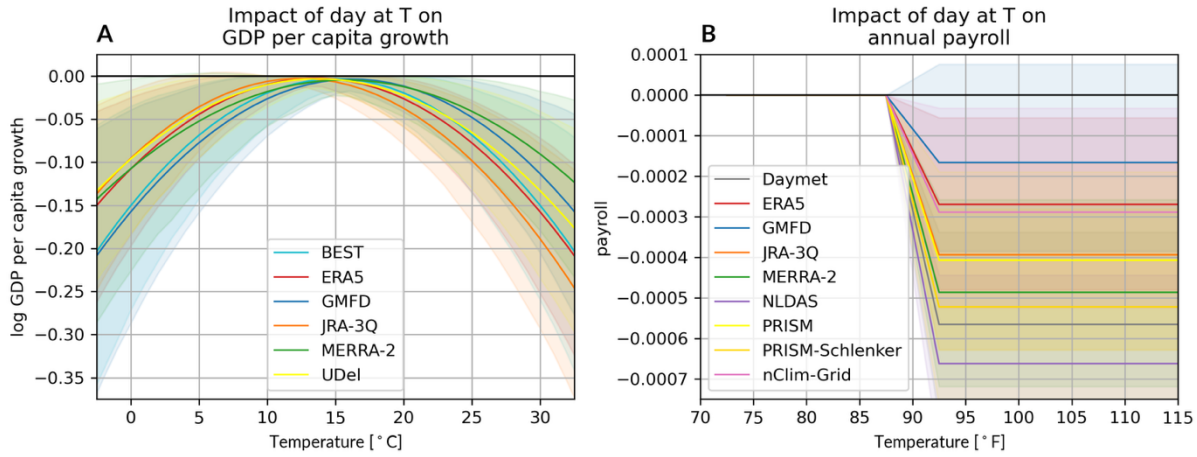


Fig. S11. Dose-response functions fit with alternate gridded historical weather records. Dose-response functions for GDP per capita growth (**A**) and annual payroll (**B**) as in main text Fig. 2, but fit using additional data products. Note that BEST provides only temperature; in A, the dose-response function fit using BEST temperature uses ERA5 precipitation. Since the GDP per capita growth model is largely insensitive to the choice of precipitation dataset (Fig. S12), this is unlikely to substantially change the fit.

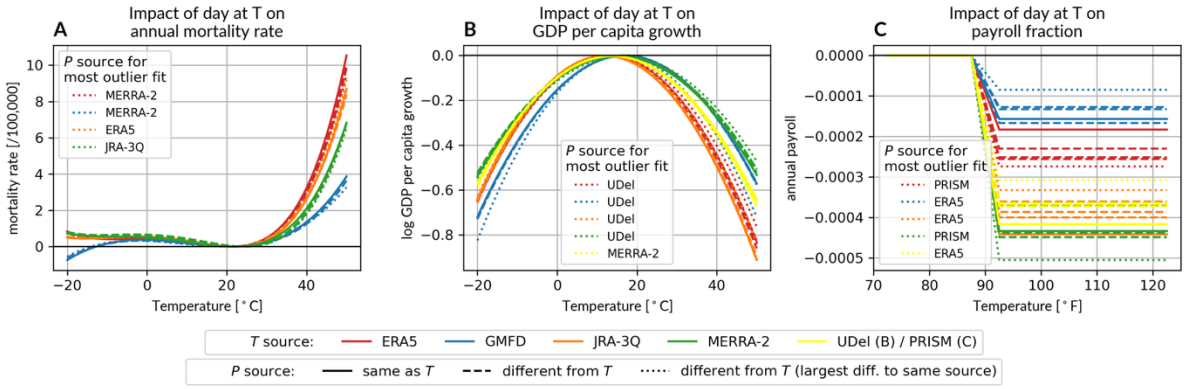


Fig. S12. Dependence of dose-response functions on precipitation dataset. Dose-response functions for mortality (**A**), GDP per capita growth (**B**), and payroll (**C**) as in main text Fig. 2 but fit using different precipitation datasets. In each panel, solid lines show dose-response functions fit using temperature and precipitation from the same gridded historical data product, while dotted lines show the same dose-response functions, but fit using precipitation taken from the other displayed historical products (e.g., the dashed red lines in A show the temperature-mortality relationship fit using temperature data from ERA5, but precipitation data from GMFD and JRA-3Q). The dose-response function that is most unlike the fit using both temperature and precipitation from the same input dataset (simply using the mean absolute difference over the domain of the figure) is shown as a dotted line (e.g., MERRA-2 for the ERA5 function in A).

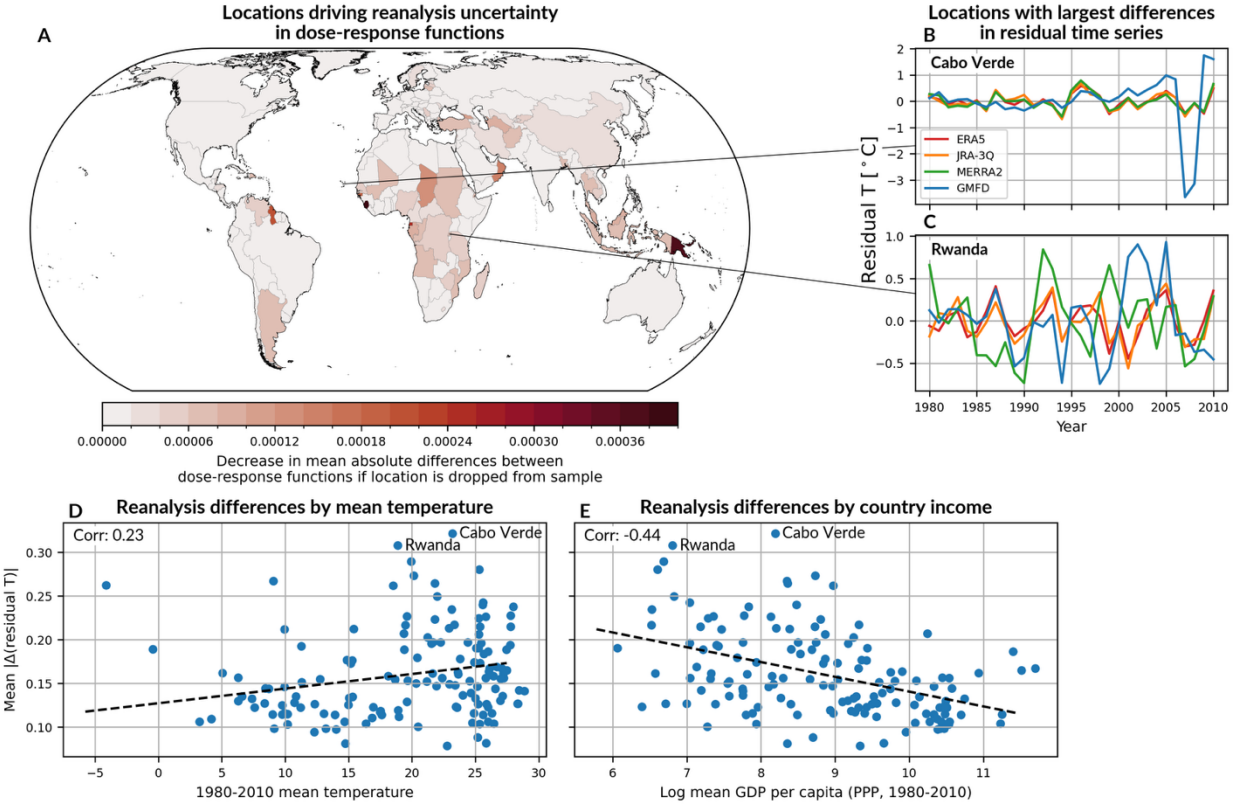


Fig. S13. Example diagnosis of reanalysis differences. Example diagnosis of the sources of reanalysis differences in fitting dose-response functions, using the GDP per capita dose-response function of Burke et al. (2015) (*40*). **(A)** Map of the reduction in differences between does-response functions when dropping a given location from the regression sample, where the difference is defined as the mean across pairs of mean absolute difference between dose-response functions fit using two different reanalyses and evaluated at the joint in-sample temperature distribution for those two reanalyses. We only show regions that, when dropped from the full all-country sample, reduce the difference between models fit using different reanalyses. Panels (**B-E**) are based on differences between residual time series at each location; the residuals are the original reanalysis time series with country and year fixed effects removed, as in the Burke et al. (2015) regression model. Panels (**B**) and (**C**) show the residual time series for Cabo Verde and Rwanda, the two locations with the largest differences between reanalyses, defined as the mean across reanalysis pairs of the mean absolute difference between time series. (**D**) This difference plotted vs. each country's 1980-2010 mean temperature. (**E**) this difference plotted vs. the log of each country's GDP per capita at purchasing power parity (from the Burke et al. (2015) (*40*) replication data).

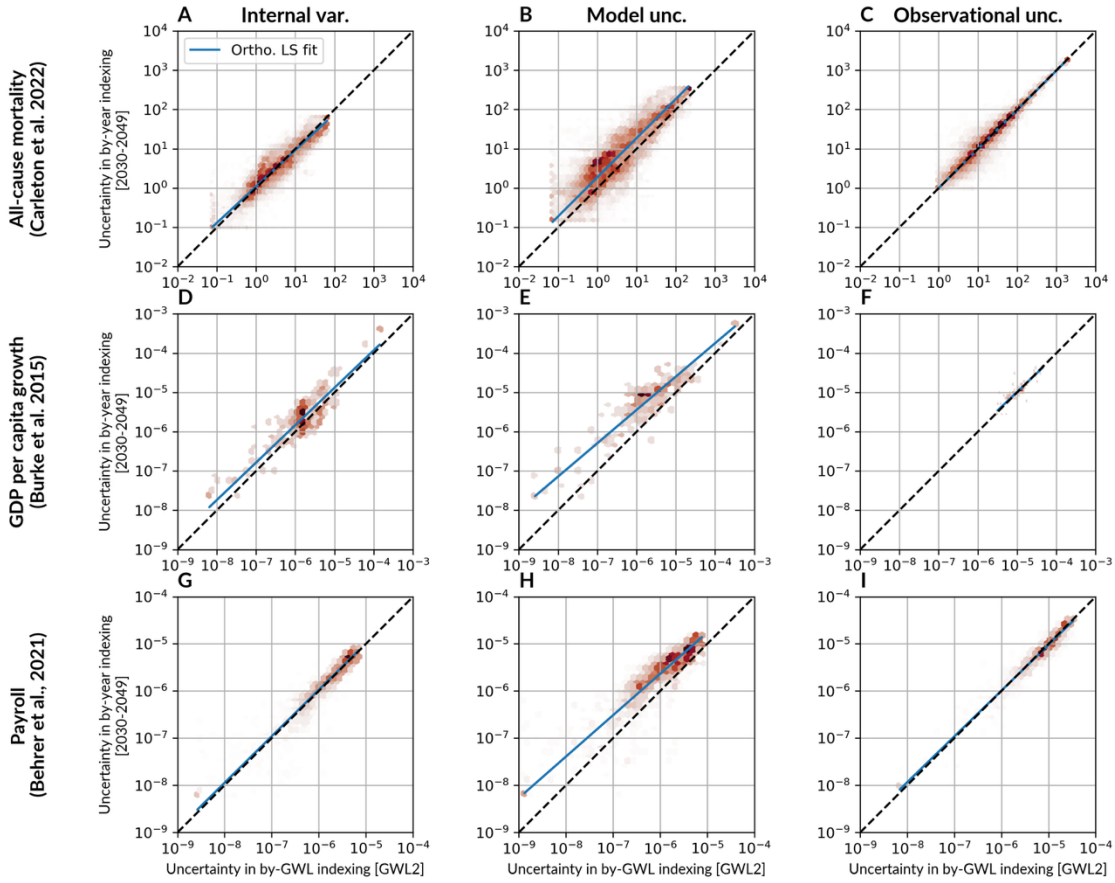


Fig. S14. Impact on climate uncertainty of normalizing projections by GWL. 2-dimensional histograms across locations of partitioned uncertainty indexed by year vs. by GWL, for each impact model and source of uncertainty. The y-axis shows uncertainties for changes between 1982-2001 and 2030-2049, the x-axis shows the same for changes between GWL0.61 and GWL2. The dashed black line is a 1:1 line, for reference. Blue lines are orthogonal least squares fits (under the assumption that uncertainty is similar in the y and the x), for reference. The average SSP2-4.5 run used passes GWL2 in 2041; the x and y axes thus on average reflect a similar change in the climate.

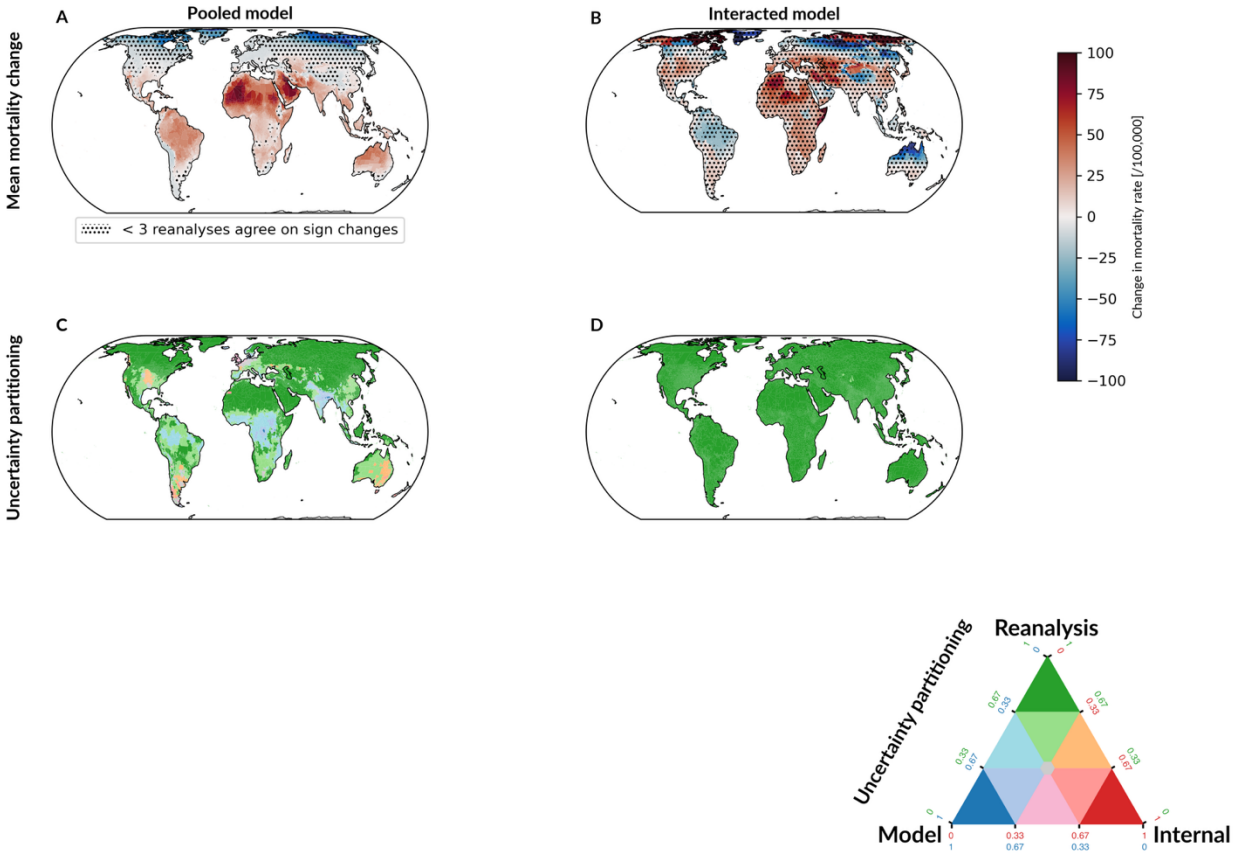


Fig. S15. Instability of the fully-interacted mortality model to reanalysis choice. Maps of mean changes (top row) and uncertainty partitioning (bottom row) of all-cause mortality rates, using the simplified 'pooled' model from Carleton et al. (2022) (*29*) (left column) as in main text figures and analysis and the fully interacted model (right column) that includes interactions with long-term local climates and GDP per capita. The interacted model is strongly unstable to the choice of historical data used to train it (possibly due to the limits of the Carleton et al. (2022) publicly available replication data, which do not include data from China and the US due to data sharing restrictions), making reanalysis uncertainty trivially dominate climate uncertainty everywhere on the globe.

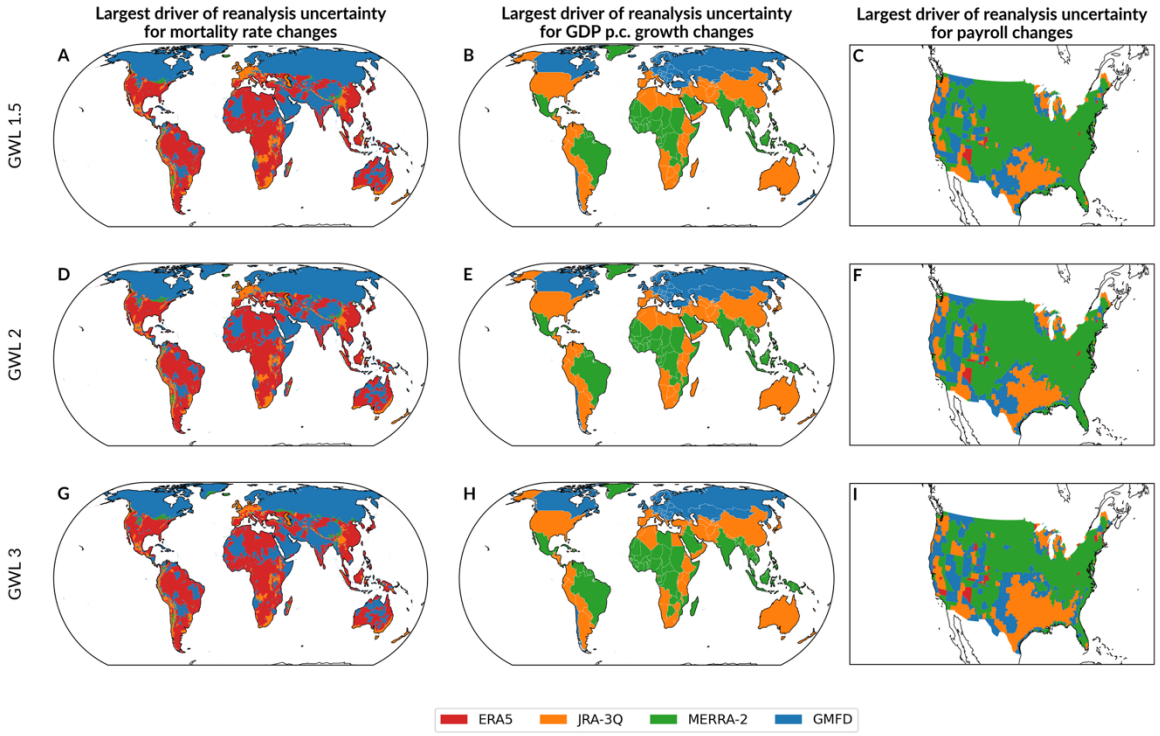


Fig. S16. Product with largest influence on reanalysis uncertainty by impact and location. The reanalysis product that is the largest driver of reanalysis uncertainty (see the supplementary materials section on the impact of individual reanalyses on estimates of observational uncertainty) for each location and impact, for projections of damages from GWL0.61 to GWL1.5 (top row), GWL2 (middle row), and GWL3 (bottom row).



Fig. S17. Dominant source of uncertainty across GWLs using all BCD-ME runs. Version of fig. S7 showing instead the largest individual source of uncertainty at each location.



Fig. S18. Dominant source of uncertainty using 1-degree historical and future climate data. Version of fig. S8 showing instead the largest individual source of uncertainty at each location.

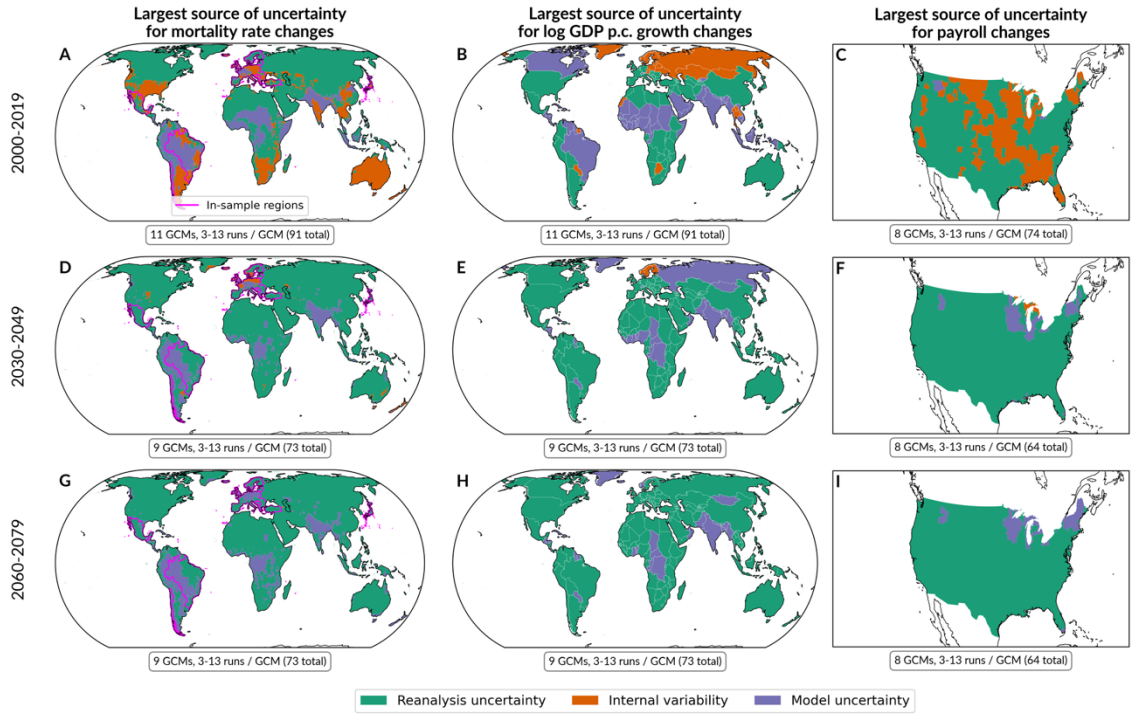


Fig. S19. Dominant source of uncertainty by year instead of by GWL. Version of fig. S9 showing instead the largest individual source of uncertainty at each location.

Data source	Publisher	Data type	Variables used	Main	Citation
Daymet	Oak Ridge National Laboratory	Statistical	Maximum daily temeprature		(*47*)
Berkeley Earth ("BEST")	Berkeley Earth	Statistical	Mean daily temeprature		(*44*)
ERA5	European Centre for Medium-Range Weather Forecasting (ECMWF)	Reanalysis	Mean and maximum daily temperature, precipitation	x	(*25*)
GMFD	Princeton Hydrology Group	Reanalysis	Mean and maximum daily temperature, precipitation	x	(*28*, *33*)
JRA-3Q	Japan Meteorological Agency (JMA)	Reanalysis	Mean and maximum daily temperature, precipitation	x	(*27*)
MERRA-2	National Aeronautic and Space Administration (NASA)	Reanalysis	Mean and maximum daily temperature, precipitation	x	(*26*)
nClimGrid	National Oceanic and Atmospheric Administration (NOAA)	Statistical	Maximum daily temeprature		(*46*)
NLDAS	NASA, NOAA, others	Reanalysis	Maximum daily temperature		(*49*)
PRISM	PRISM Climate Group, Oregon State University	Statistical	Maximum daily temperature, precipitation		(*48*)
Fine-scaled weather dataset ("PRISM-Schlenker")	Wolfram Schlenker	Statistical	Maximum daily temeprature		(*59*)
Willmott and Matsuura ("UDel")	University of Delaware	Statistical	Mean daily temperature, precipitation		(*69*)

Table S*4* Gridded historical climate data products used. "Reanalysis" products use physics-informed weather or land models constrained by observations; "stastical" products gapfill observations with models of varying degrees of complexity, ranging from pure interpolations to models informed by topography or other local characteristics. Names in quotes and parentheses are shorthands for a given product used in Main Text and Supplementary Figures.

Variable	GWL reached: / Model	1.0	1.5	2.0	2.5	3.0	3.5	4.0
tas	ACCESS-CM2	1	1	1	1	1	1	0
	ACCESS-ESM1-5	23	23	23	23	5	5	5
	BCC-CSM2-MR	2	2	2	2	2	1	0
	BCC-ESM1	1	1	0	0	0	0	0
	CAMS-CSM1-0	1	1	1	1	0	0	0
	CESM2-WACCM	8	8	8	7	7	4	3
	CMCC-CM2-SR5	1	1	1	1	1	1	1
	CMCC-ESM2	1	1	1	1	1	1	1
	CNRM-CM6-1	18	18	18	18	15	12	6
	CNRM-ESM2-1	41	41	31	26	13	7	5
	CanESM5	86	86	86	86	86	86	79
	EC-Earth3	35	35	35	35	32	15	10
	EC-Earth3-Veg	13	13	13	13	13	9	6
	FGOALS-g3	10	10	10	7	3	0	0
	IITM-ESM	1	1	1	1	1	0	0
	IPSL-CM6A-LR	25	25	25	25	25	15	14
	MIROC-ES2L	1	1	1	1	1	0	0
	MIROC6	60	34	34	31	28	0	0
	MPI-ESM-1-2-HAM	1	1	0	0	0	0	0
	MPI-ESM1-2-LR	30	30	30	20	16	6	0
	MRI-ESM2-0	12	8	8	8	7	2	0
	NESM3	1	1	1	1	1	1	1
	Total	372	342	330	308	258	166	131
tasmax	ACCESS-CM2	1	1	1	1	1	1	1
	ACCESS-ESM1-5	6	6	6	6	6	6	6
	BCC-CSM2-MR	1	1	1	1	1	1	0
	BCC-ESM1	1	1	0	0	0	0	0
	CAMS-CSM1-0	1	1	1	1	0	0	0
	CMCC-ESM2	1	1	1	1	1	1	1
	CNRM-CM6-1	5	5	5	3	2	2	1
	CNRM-ESM2-1	5	5	3	3	2	1	1
	CanESM5	30	30	30	30	30	30	27
	EC-Earth3	22	22	22	22	19	8	3
	EC-Earth3-Veg	10	10	10	10	10	5	2
	FGOALS-g3	7	7	7	4	0	0	0
	IPSL-CM6A-LR	22	22	22	22	22	12	11
	MIROC-ES2L	2	2	2	2	1	0	0
	MIROC6	37	25	25	22	19	0	0
	MPI-ESM-1-2-HAM	1	1	0	0	0	0	0
	MPI-ESM1-2-LR	30	30	30	20	16	6	0
	MRI-ESM2-0	16	16	16	14	11	6	0
	NESM3	1	1	1	1	1	1	1
	Total	199	187	183	163	142	80	54

Table S5 Number of ensemble members by GCM used. with how many runs have data for at least a given GWL, for near-surface mean daily air temperature (`tas`, top half, used for mortality and GDP per capita growth calculations) and near-surface maximum daily air temperature (`tasmax`, bottom half, used for payroll calculations). Models with more than 8 runs are the 'Large Ensembles' used in primary results; other models are used to verify model uncertainty in fig. S6**.**